Crystal chemical constraints on inter-mineral Fe isotope fractionation and implications for Fe isotope disequilibrium in San Carlos mantle xenoliths

Catherine A. Macris [*], Craig E. Manning, Edward D. Young

Department of Earth, Planetary, and Space Sciences, University of California at Los Angeles, Los Angeles, CA 90095-1567, USA

Abstract

The origin of variations in iron isotope compositions of mantle minerals is uncertain, and predictions of equilibrium inter-mineral iron isotope fractionation conflict. This hinders interpretation of the petrologic and geochemical implications of Fe isotope data from mantle lithologies. To address this, we present a revised ionic model for predicting equilibrium iron isotope fractionation between mantle minerals and use it to interpret measured inter-mineral iron isotopic fractionation from five distinct mantle xenolith lithologies from San Carlos, Arizona. The samples represent a broad range of modal abundances and include lherzolite, harzburgite, dunite, clinopyroxenite, and websterite. The xenoliths exhibit Fe-isotopic variation between minerals in a single sample, and between samples. In all cases where spinel and olivine coexist, the $^{57}Fe/^{54}Fe$ of spinel is greater than that of the corresponding olivine, agreeing with expectations for equilibrium fractionation from theory (ionic model), but disagreeing with predictions based on Mössbauer data. The $^{57}Fe/^{54}Fe$ values of clinopyroxenes from the xenoliths show no clear systematic differences. We interpret this to be a result of varying degrees of metasomatism, perhaps involving inter-action with a melt. The spinel peridotite samples (lherzolite, harzburgite, and dunite) are partially melted residual mantle that exhibit a decrease in whole-rock $^{57}Fe/^{54}Fe$ with increasing olivine abundance. This is consistent with progressive extraction of a ^{57}Fe-rich partial melt. The clinopyroxenite has the highest whole-rock $^{57}Fe/^{54}Fe$, consistent with its origin as a cumulate from an unrelated magma possessing elevated $^{57}Fe/^{54}Fe$. The websterite sample is transitional to Group II type xenoliths, has the lowest whole-rock $^{57}Fe/^{54}Fe$ of the investigated samples, and likely experienced a more complex metasomatic history. This study demonstrates that the Fe isotope compositions of San Carlos xenoliths and their component minerals record the complex petrologic history and local heterogeneity of the subcontinental mantle lithosphere.
© 2015 Elsevier Ltd. All rights reserved.

1. INTRODUCTION

Iron stable isotope ratios have the potential to be powerful tracers for geochemical processes in the mantle, such as partial melting, metasomatism, and oxidation. Precise determination of inter-mineral fractionation of iron iso-

topes in these rocks is the key to applying these tracers successfully. Although the data available for iron isotope compositions of mantle minerals are growing and substantial, the data taken as a whole do not provide a coherent picture of the underlying systematics governing high temperature Fe isotope fractionation between minerals. Iron isotope ratios of mantle xenolith minerals reported in previous studies vary within a single sample as well as between xenoliths (Zhu et al., 2002; Beard and Johnson, 2004; Poitrasson et al., 2004, 2013; Williams et al., 2004, 2005, 2009; Schoenberg and von Blanckenburg, 2006; Weyer

* Corresponding author at: Division of Geological and Planetary Sciences, California Institute of Technology, Pasadena, CA 91125, USA.

E-mail address: camacris@caltech.edu (C.A. Macris).

et al., 2005; Weyer and Ionov, 2007; Dauphas et al., 2009; Zhao et al., 2010, 2012; Huang et al., 2011). The confusion is exacerbated by incomplete understanding of equilibrium inter-mineral Fe isotope fractionation.

Williams et al. (2005) found significant variations in $^{57}Fe/^{54}Fe$ of a large suite of mantle rocks and their constituent minerals, resulting in some ambiguity concerning the fractionation of iron isotopes between the different phases. For example, the study showed that in some mantle rocks, spinel has greater $^{57}Fe/^{54}Fe$ values than olivine, whereas in other rocks olivine has the higher $^{57}Fe/^{54}Fe$ values, implying local isotopic disequilibrium. Iron isotope data from Zhu et al. (2002) also showed some variation in the $^{57}Fe/^{54}Fe$ of mantle olivine and clinopyroxene from three different xenoliths. Zhu et al. did not measure the iron isotopic compositions of spinels and only report orthopyroxene Fe isotope ratios for two out of three, finding no systematic fractionation. Clearer trends have emerged for clinopyroxene–garnet pairs from mantle rocks. Beard and Johnson (2004) and Williams et al. (2009) found clinopyroxene with higher $^{57}Fe/^{54}Fe$ than coexisting garnet in eclogite xenoliths and garnet peridotites, for example. Zhao et al. (2010, 2012) measured small but distinguishable Fe isotopic variations in spinel lherzolites and clinopyroxenites from the North China Craton. Their inter-mineral Fe isotope fractionation measurements showed no clear systematics within individual xenoliths. On the other hand, a recent study by Williams and Bizimis (2014) found that Fe isotope values of clinopyroxenes in Hawaiian peridotites and pyroxenites were always heavier than, or within error of, coexisting olivine and garnet, respectively. In summary, the current inter-mineral Fe isotope fractionation data set exhibit often conflicting or ambiguous trends regarding the degree of enrichment of heavy iron isotopes among constituent minerals (Fig. 1).

The variability in iron isotope compositions of mantle minerals from different areas may be due in part to the intrinsic petrologic variability inherent in different sample localities. For example the samples measured by Williams et al. (2005) come from very diverse petrological locales, including sub-continental margin mantle, sub-continental mantle lithosphere, and sub-arc mantle. A recent study by Poitrasson et al. (2013) highlights iron isotope heterogeneity of lithospheric mantle xenoliths from different geodynamic settings. They concluded that metasomatism by low viscosity melts/fluids, not partial melting processes, is the main cause of the large range of Fe isotope values in mantle minerals. Williams and Bizimis (2014) also point to mantle heterogeneity to explain differences in MORB and OIB Fe isotope measurements, but they attribute the heterogeneity to fractional crystallization and cumulate forming processes as opposed to metasomatism.

Evaluation of the origins of the discrepancies in inter-mineral fractionations is further hindered by disagreement between predictions for the signs and magnitudes of fractionation factors. Qualitative rules governing equilibrium stable isotope fractionation (e.g., Schauble, 2004; Young et al., 2009) suggest that spinel should concentrate the heavy isotopes of iron relative to olivine and pyroxenes. The opposite is found by modeling of Mössbauer data
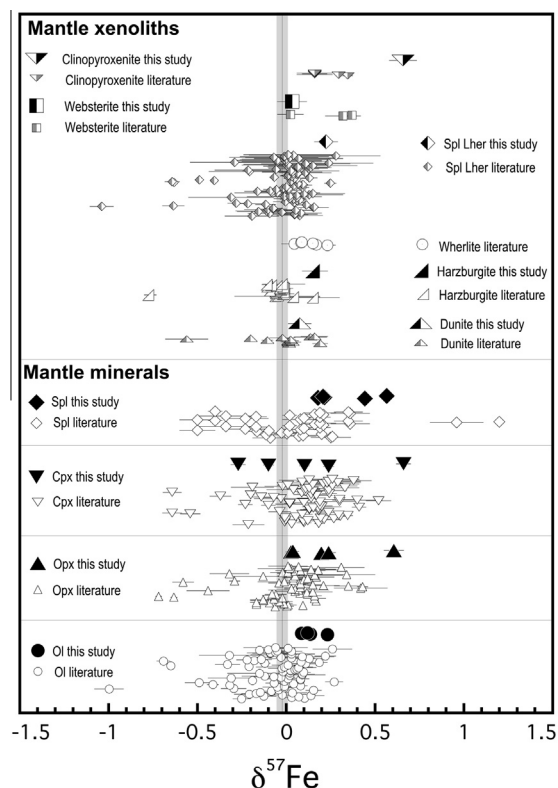

Fig. 1. Fe isotope compositions of mantle minerals and xenoliths from this and previous studies. The solid line represents the mean of mantle xenolith data presented here, and the gray band represents 2 standard deviations of the mean uncertainty. Data from Zhu et al. (2002), Beard and Johnson (2004), Poitrasson et al. (2004, 2013), Williams et al. (2004, 2005), Weyer et al. (2005), Schoenberg and von Blanckenburg (2006), Weyer and Ionov (2007), Dauphas et al. (2009), Zhao et al. (2010, 2012), Huang et al. (2011); and this study (Table 2). Ol, olivine; Opx, orthopyroxene; Cpx, clinopyroxene; Spl, spinel; Spl Lher, Spinel Lherzolite.

(Polyakov, 1997; Polyakov and Mineev, 2000). These opposing predictions, combined with the variability seen so far in natural samples, raise important questions about sources of Fe isotope variability in the mantle. These questions will only be answered with a better understanding of equilibrium Fe isotope fractionation factors among the relevant phases.

We measured inter-mineral iron isotopic fractionation of minerals from the well-characterized mantle xenoliths from San Carlos, Arizona, in order to better understand high temperature inter-mineral iron isotope fractionation and its controls in a single, well studied xenolith suite. San Carlos xenoliths are among the most widely studied samples of mantle lithosphere because they are abundant and easily sampled, and they form a coherent, well-understood and representative petrologic record of mantle lithospheric processes (Frey and Prinz, 1978; Galer and O'Nions, 1988). Our goals are to determine the fractionation of iron isotopes between the minerals spinel, olivine, orthopyroxene, and clinopyroxene, interpret the observed fractionations in light of the crystal chemical

principles that apply to these mineral structures, and place the data in the context of the petrologic evolution of the subcontinental mantle lithosphere.

2. GEOLOGICAL BACKGROUND AND SAMPLE DESCRIPTION

The ultramafic xenoliths used in this study are from San Carlos, Arizona, USA. San Carlos ultramafic xenoliths occur mostly as gravity settled masses exposed in lower parts of the ~500 Ka basanite flow/vent complex of Peridot Mesa (e.g., Holloway and Cross, 1978; Bernatowicz, 1981). Most xenoliths can be classified into one of two groups, commonly referred to as Groups I and II (Frey and Prinz, 1978). Detailed compositional characteristics of these two groups can be found in the Supplementary material (Appendix A). Group I xenoliths are dominated by olivine-rich peridotites with compositional features of melt extraction (Frey and Prinz, 1978). Some of these rocks show trace-element and isotopic evidence of subsequent metasomatism (Frey and Prinz, 1978; Galer and O'Nions, 1989; Menzies, 2003). The pyroxene-rich lithologies include orthopyroxenites, websterites, and clinopyroxenites with varying olivine contents. The orthopyroxene-rich Group I rocks are interpreted as either residual tectonic layer in peridotites, or as cumulates from the extracted basaltic liquid. Clinopyroxene-rich rocks may occur as layers or veins in lherzolites, or as discrete xenoliths, and possess the geochemical signatures of equilibration with alkaline mafic magma prior to transport to the surface (Frey and Prinz, 1978).

Group II xenoliths are highly variable in terms of mineral proportions and compositions, including spinel clinopyroxenites and spinel olivine websterites. Kaersutitic amphibole is common. They are interpreted as cumulates from a SiO_2-undersaturated magma, most likely the host

basanite (Frey and Prinz, 1978). In this study, five lithologically distinct xenoliths were studied: spinel lherzolite, spinel harzburgite, spinel dunite, clinopyroxenite, and olivine websterite. To assess Fe isotope systematics of the local mantle lithosphere prior to modification from the magmatic event that brought them to the surface, we mostly focused on Group I xenoliths with four analyzed samples clearly identified as Group I xenolith and one sample (olivine websterite) identified as transitional between the two groups (Fig. 2). Thin sections of each xenolith were analyzed by petrographic microscope and electron probe microanalyzer (EPMA) to determine mineral textures, modes, and compositions (Table 1). Representative backscattered electron images of each xenolith are presented in Supplementary Fig. 1.

The three peridotite xenoliths chosen for this study represent a wide range of olivine abundance, including a spinel lherzolite (CEM1-3), a harzburgite (111-312-37), and a dunite (111-312-26). Two pyroxene-rich xenoliths were also analyzed: a clinopyroxenite (SC-1-66), and an olivine websterite (SC-1-70). Mineral mode, Mg #, and $Fe^{3+}/\sum Fe$ for all minerals in the xenoliths are given in Table 1. See Supplementary material for methods of determining these values and for a more detailed discussion of the background and samples.

3. METHODS FOR STABLE ISOTOPIC ANALYSIS

Minerals were separated from the five xenoliths by handpicking with the aid of a binocular microscope. The identity of each grain was confirmed by energy dispersive X-ray analysis using a scanning electron microscope (SEM) prior to dissolution. Mineral separates were weighed, then powdered in an agate mortar and pestle, and subsequently dissolved in two steps using the method described in Young et al. (2009). The iron was purified by
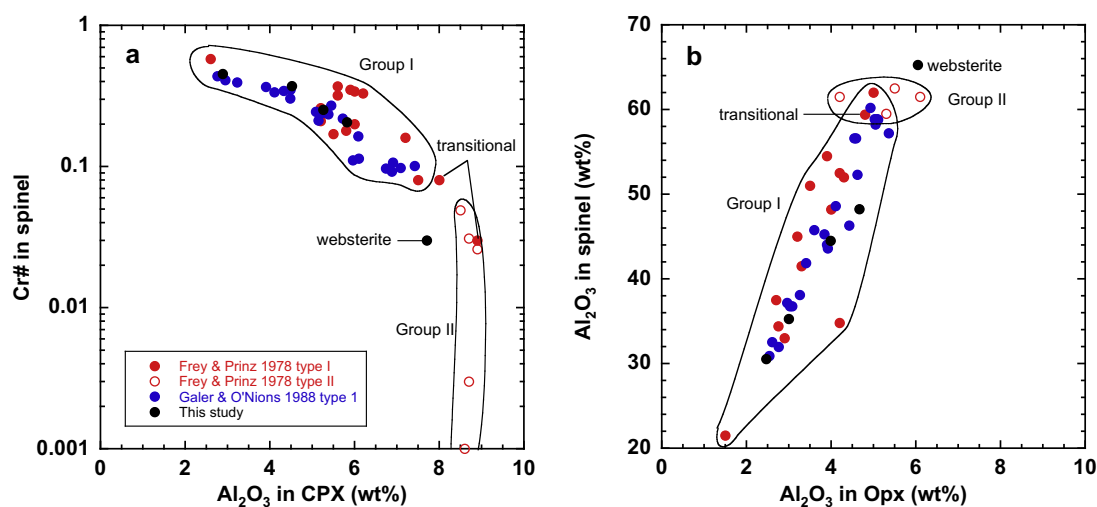

Fig. 2. Classification of Groups I and II xenoliths from San Carlos, AZ. Data from this study are black solid circles. Open and closed red circles are data from Frey and Prinz (1978). Closed blue circles are from Galer and O'Nions (1988). (a) Chromium number in spinels versus aluminum oxide content of clinopyroxenes. (b) Weight percent aluminum oxide in spinels versus orthopyroxenes. The websterite sample from this study does not fall into a clearly defined region for either Group I or II. (For interpretation of the references to color in this figure legend, the reader is referred to the web version of this article.)

Table 1

Average mineral compositions[a] in peridotite and pyroxenite xenoliths from San Carlos, AZ.

Sample	SC-1-66			CEM1-3				111.312.37				111-312-26				SC-1-70			
Rock	Clinopyroxenite			Spinel lherzolite				Harzburgite				Dunite				Websterite			
Mineral[b]	Opx	Cpx	Spl	Ol	Opx	Cpx	Spl	Ol	Opx	Cpx	Spl	Ol	Opx	Cpx	Spl	Ol	Opx	Cpx	Spl
n[c]	28	16	20	66	16	34	36	11	9	12	8	11	9	15	19	14	17	19	2
SiO_2	55.04	51.73	0.04	40.25	54.60	52.67	0.02	41.01	56.30	52.88	0.02	40.89	54.76	51.44	0.05	40.14	53.65	50.94	0.05
TiO_2	0.17	0.51	0.35	0.01	0.14	0.12	0.12	0.03	0.03	0.33	0.18	0.04	0.08	0.55	0.13	0.01	0.11	0.40	0.10
Al_2O_3	4.07	5.32	44.26	0.01	5.34	4.52	35.28	0.02	2.48	3.20	30.58	0.03	4.68	5.60	48.33	0.03	6.02	7.54	65.28
Cr_2O_3	0.64	1.27	22.99	0.02	0.38	1.44	32.64	0.03	0.60	1.19	39.51	0.04	0.65	1.06	19.24	0.03	0.15	0.24	2.91
Fe_2O_3	0.67	0.23	1.89	0.38	1.15	0.69	3.02	0.67	0.74	0.61	2.40	0.32	0.78	1.25	1.98	1.09	1.06	1.22	1.38
FeO	6.00	2.81	11.97	8.71	5.90	2.13	11.37	8.00	4.73	2.09	11.50	8.48	4.77	2.25	9.31	11.46	6.77	2.74	10.43
MnO	0.16	0.10	0.18	0.13	0.16	0.09	0.24	0.13	0.13	0.11	0.24	0.14	0.13	0.11	0.15	0.17	0.17	0.12	0.12
MgO	32.69	16.27	17.65	48.94	32.21	15.73	17.01	50.61	34.21	17.54	16.79	49.98	32.90	16.13	19.64	47.50	31.11	15.48	21.18
CaO	0.91	20.65	0.01	0.07	0.92	19.65	0.00	0.07	0.93	20.90	0.01	0.10	1.05	20.19	0.01	0.10	1.00	19.55	0.02
Na_2O	0.05	0.83	0.01	0.00	0.15	1.65	0.00	0.02	0.04	0.69	0.01	0.02	0.11	1.06	0.02	0.01	0.10	1.23	0.00
K_2O	0.01	0.01	0.01	0.00	0.01	0.00	0.00	0.01	0.01	0.01	0.01	0.02	0.02	0.01	0.01	0.01	0.00	0.01	0.01
NiO	0.09	0.05	0.28	0.00	0.00	0.00	0.00	0.39	0.09	0.05	0.19	0.37	0.09	0.06	0.32	0.35	0.10	0.05	0.40
Sum	100.51	99.78	99.64	98.51	100.96	98.69	99.70	100.99	100.29	99.61	101.44	100.40	100.02	99.70	99.18	100.89	100.24	99.52	101.88
Tetrahedral cations[d]																			
Si	1.898	1.881	0.000	0.998	1.874	1.927	0.001	0.993	1.934	1.922	0.001	0.997	1.890	1.871	0.001	0.990	1.862	1.852	0.001
Al	0.102	0.119	0.000	0.000	0.126	0.073	0.000	0.000	0.066	0.078	0.000	0.001	0.110	0.129	0.000	0.001	0.138	0.148	0.000
Fe^{2+}	0.000	0.000	0.277	0.000	0.000	0.000	0.272	0.000	0.000	0.000	0.277	0.000	0.000	0.000	0.211	0.000	0.000	0.000	0.217
Mg	0.000	0.000	0.727	0.000	0.000	0.000	0.725	0.000	0.000	0.000	0.721	0.000	0.000	0.000	0.790	0.000	0.000	0.000	0.784
Octahedral cations																			
Ti	0.004	0.014	0.007	0.000	0.004	0.003	0.003	0.000	0.001	0.009	0.004	0.000	0.002	0.015	0.003	0.000	0.003	0.011	0.002
Al	0.064	0.109	1.442	0.000	0.090	0.122	1.190	0.000	0.034	0.059	1.039	0.000	0.080	0.111	1.540	0.000	0.109	0.174	1.911
Cr	0.017	0.036	0.502	0.000	0.010	0.042	0.739	0.000	0.016	0.034	0.900	0.001	0.018	0.030	0.412	0.001	0.004	0.007	0.057
Fe^{3+}	0.017	0.006	0.039	0.007	0.030	0.019	0.065	0.012	0.019	0.017	0.052	0.006	0.016	0.034	0.040	0.020	0.028	0.033	0.026
Fe^{2+}	0.173	0.085	0.000	0.181	0.169	0.065	0.000	0.162	0.136	0.064	0.000	0.173	0.142	0.068	0.000	0.236	0.197	0.083	0.000
Mn	0.005	0.003	0.004	0.003	0.005	0.003	0.006	0.003	0.004	0.003	0.006	0.003	0.004	0.003	0.003	0.003	0.005	0.004	0.000
Mg	1.681	0.882	0.000	1.809	1.648	0.858	0.000	1.827	1.752	0.950	0.000	1.817	1.693	0.875	0.000	1.747	1.610	0.839	0.000
Ca	0.034	0.804	0.000	0.002	0.034	0.770	0.000	0.000	0.034	0.814	0.000	0.003	0.039	0.787	0.001	0.003	0.037	0.761	0.003
Na	0.004	0.059	0.000	0.000	0.010	0.117	0.000	0.006	0.003	0.049	0.000	0.000	0.007	0.075	0.006	0.000	0.007	0.087	0.001
K	0.000	0.000	0.000	0.000	0.001	0.000	0.000	0.003	0.000	0.001	0.000	0.000	0.001	0.001	0.001	0.000	0.000	0.000	0.002
Ni	0.003	0.001	0.036	0.000	0.000	0.000	0.000	0.006	0.003	0.001	0.000	0.000	0.003	0.002	0.042	0.000	0.003	0.002	0.048
Sum	4.002	4.001	3.034	3.000	4.000	4.000	3.000	3.013	4.002	4.001	3.001	3.001	4.004	4.001	3.050	3.001	4.002	4.001	3.051
Modal[e]	0.05	0.95	<0.01	0.64	0.24	0.12	<0.01	0.69	0.27	0.04	<0.01	0.93	0.02	0.05	<0.01	0.32	0.58	0.1	<0.01
Mg#[f]	0.90	0.91	0.70	0.91	0.89	0.91	0.68	0.91	0.92	0.92	0.69	0.91	0.91	0.90	0.76	0.87	0.88	0.88	0.76
$Fe^{3+}/\sum Fe$	0.09	0.07	0.12	–	0.15	0.22	0.19	–	0.12	0.21	0.16	–	0.10	0.33	0.16	–	0.12	0.29	0.11
2σ[g]	0.03	0.08	0.07		0.03	0.08	0.09		0.06	0.54	0.01		0.04	0.55	0.02		0.02	0.05	0.04

[a] Major oxide compositions measured on a JEOL Superprobe microanalyzer with five spectrometers using an accelerating voltage of 15 kv, 15 nA current, 20 s counting time, and focused beam.

[b] Abbreviations: Ol, olivine; Opx, orthopyroxene; Cpx, clinopyroxene; Spl, spinel.

[c] n = number.

[d] Cation occupancies based on recalculating probe data determined by charge balance assuming no vacancies. Cation proportions based on six oxygens for Opx and Cpx, and four oxygens for Ol and Spl.

[e] Mineral mode determined by point counting and EPMA analyses.

[f] Mg# = Mg/(Mg + Fe$_{Total}$).

[g] Errors on ferric iron estimates are reported as 2 standard deviations (see Supplementary material for methods).

anion exchange chromatography in HEPA filtered laminar flow boxes within a class 100 clean laboratory using a one-column procedure (described in detail in the Supplementary material).

Iron isotope ratio measurements were made using a ThermoFinnigan Neptune MC-ICPMS. The instrument has a fixed array of 9 Faraday collectors each with amplifier resistors of 10^{11} Ω. Sample purity was checked by monitoring $^{23}Na^+$, $^{24}Mg^+$, $^{27}Al^+$, $^{44}Ca^+$, $^{52}Cr^+$, $^{55}Mn^+$ and $^{58}Ni^+$. In all cases, after purification by column chemistry, the abundances of these potential impurities were <1% (atomic) of the analyte Fe concentration. Such low impurity/Fe ratios are well below thresholds for discernible matrix effects on Fe isotope ratio measurements as determined by tests using various mixtures of these elements against pure Fe solutions.

Samples and standard were analyzed as ~1 ppm Fe in 2% HNO_3 aspirated through a Cetac Aridus II® desolvat-

ing nebulizer (samples were run in dry plasma) with the addition of N_2.. Mass interferences from ArO^+ (~2.5 mV), $ArOH^+$ (<1 mV), and ArN^+ (~1.8 V) were resolved from $^{56}Fe^+$, $^{57}Fe^+$ and $^{54}Fe^+$, respectively, by operating at a high mass resolving power of $m/\Delta m > 10,000$ (Weyer and Schwieters, 2003). Corrections for instrumental mass bias were obtained by using sample-standard bracketing with peak height matching between sample and standard to better than 5%. Samples were analyzed 8–10 times with each analysis consisting of 20 cycles of ~4 s integrations.

All values for Fe isotope ratios presented here were obtained by comparison with the international Fe standard, IRMM-014, (Beard and Johnson, 2004) and are reported in the conventional delta notation:

$$\delta^i Fe = 10^3 \left(\frac{(^iFe/^{54}Fe)_{Sample}}{(^iFe/^{54}Fe)_{IRMM-14}} - 1 \right) \quad (1)$$

Table 2
Iron isotopic compositions of whole-rocks and minerals from peridotite and pyroxenite xenoliths from San Carlos, AZ.

Sample	Rock type	Mineral[a]	δ57Fe	2 SE	δ56Fe	2 SE	n[b]
CEM1-3	Spl Lherzolite	Cpx	0.26	0.02	0.16	0.04	8
		Cpx duplicate[c]	0.21	0.01	0.13	0.01	8
		Cpx average[d]	**0.24**	**0.02**	**0.15**	**0.02**	
		Opx	0.18	0.01	0.11	0.01	8
		Opx duplicate	0.22	0.02	0.14	0.03	8
		Opx average	**0.20**	**0.04**	**0.12**	**0.03**	
		Ol	0.21	0.02	0.12	0.03	8
		Ol duplicate	0.25	0.02	0.18	0.03	8
		Ol average	**0.23**	**0.04**	**0.15**	**0.06**	
		Spl	0.42	0.02	0.27	0.01	8
		Spl duplicate	0.46	0.01	0.30	0.01	8
		Spl average	**0.44**	**0.04**	**0.29**	**0.03**	
		Whole-rock[e]	0.22	0.03	0.05	0.02	
		Whole-rock[f]	0.19	0.10	0.11	0.08	8
111-312-37	Harzburgite	Cpx	0.10	0.03	0.04	0.02	8
		Opx	0.24	0.04	0.17	0.01	8
		Ol	0.14	0.04	0.10	0.02	8
		Spl	0.18	0.03	0.01	0.02	7
		Whole-Rock[e]	0.16	0.03	0.05	0.01	
111-312-26	Dunite	Cpx	−0.10	0.03	−0.14	0.01	9
		Opx	0.03	0.03	−0.01	0.02	7
		Ol	0.09	0.03	0.04	0.01	9
		Spl	0.22	0.04	0.11	0.03	7
		Whole-rock[e]	0.07	0.03	−0.01	0.02	
SC-1-70	Websterite	Cpx	−0.27	0.04	−0.27	0.03	9
		Opx	0.04	0.03	0.00	0.02	8
		Ol	0.06	0.03	0.26	0.03	8
		Spl	0.21	0.05	0.11	0.04	7
		Whole-rock[e]	0.03	0.02	−0.01	0.02	
SC-1-66	Clinopyroxenite	Cpx	0.66	0.04	0.46	0.03	8
		Opx	0.61	0.05	0.41	0.02	8
		Spl	0.57	0.03	0.36	0.03	7
		Whole-rock[e]	0.66	0.04	0.46	0.03	

[a] Abbreviations: Cpx, clinopyroxene; Opx, orthopyroxene; Ol, olivine; Spl, spinel.
[b] n = number of replicate analyses performed.
[c] Duplicate = a second aliquot of the sample was dissolved, purified, and analyzed by MC-ICP-MS.
[d] Average = the average of the above mineral and duplicate analysis (shown in bold). Errors here represent our external reproducibility.
[e] Whole-rock Fe isotopic compositions calculated based on mineral separate data and modal mineralogy (Table 1).
[f] Whole-rock Fe isotopic compositions measured directly.

where i refers to 56 or 57. The aliquot of IRMM-14 for this work was stored as a 20 ppm solution of Fe in HNO_3, stored in a Teflon® bottle and was analyzed each day against an internal standard (Spex CertiPrep™ Fe standard solution) during the course of this study. Based on 34 separate measurements of IRMM-14 against the internal standard, our long-term external reproducibility for the data presented here is $\delta^{56}Fe = \pm 0.04$ and $\delta^{57}Fe = \pm 0.06$ (2 standard deviations). Two standard deviations of the mean of all 34 measurements (2 standard error) yields ± 0.01 and $= \pm 0.02$ for $\delta^{56}Fe$ and $\delta^{57}Fe$, respectively. Internal uncertainties in all $\delta^i Fe$ values of minerals and bulk rocks are given in Table 2 at the 2 standard error level, as determined from multiple analyses of analyte solutions. Duplicate analyses of minerals from Spl lherzolite CEM1-3 are also reported in Table 2. The duplicate analyses (Table 2) agree with our reported estimates of long-term external precision.

4. RESULTS

Iron isotopic compositions for individual minerals and whole rocks are presented in Table 2 and Fig. 3. In describing our results we use $\delta^{57}Fe$ rather than $\delta^{56}Fe$, although both are reported to allow comparison to previous work and demonstrate adherence to mass dependent fractionation. The whole-rock Fe isotopic compositions (WR) were calculated from the measured iron isotope ratios of the constituent minerals of these xenoliths and their mineral modal abundances (Table 1). In the case of the spinel lherzolite (CEM1-3), we also measured the whole-rock Fe isotopic composition directly from an aliquot of powdered bulk rock. The measured value of $0.19 \pm 0.10‰$ agrees with the calculated value of $0.22 \pm 0.03‰$ within uncertainties, giving us confidence in our reconstructed whole rock values. The $\delta^{57}Fe$ values of whole rocks range from $0.03‰$

to $0.66‰$ (Table 2). With the exception of the websterite, the whole rock $\delta^{57}Fe$ decrease with increasing olivine content of the rocks (Fig. 3).

In every case where a rock contains both olivine and spinel (every sample except the clinopyroxenite), the spinel is enriched in the heavy isotopes of iron relative to coexisting olivine (Fig. 3). Clinopyroxene does not appear to exhibit any clear systematic behavior regarding $^{57}Fe/^{54}Fe$ relative to other phases. The order of $^{57}Fe/^{54}Fe$ of constituent minerals from the spinel lherzolite (CEM1-3) is $\delta^{57}Fe_{Spl} > \delta^{57}Fe_{Cpx} \geqslant \delta^{57}Fe_{Ol} \geqslant \delta^{57}Fe_{Opx}$. For harzburgite (111-312-37), we obtain $\delta^{57}Fe_{Opx} > \delta^{57}Fe_{Spl} > \delta^{57}Fe_{Ol} > \delta^{57}Fe_{Cpx}$. For dunite (111-312-26) we measured $\delta^{57}Fe_{Spl} > \delta^{57}Fe_{Ol} > \delta^{57}Fe_{Opx} > \delta^{57}Fe_{Cpx}$. The websterite (SC-1-70) is similar to dunite and yields $\delta^{57}Fe_{Spl} > \delta^{57}Fe_{Ol} \geqslant \delta^{57}Fe_{Opx} > \delta^{57}Fe_{Cpx}$. Lastly, the clinopyroxenite (SC-1-66) stands out from the others with the apparent order: $\delta^{57}Fe_{Cpx} \geqslant \delta^{57}Fe_{Opx} \geqslant \delta^{57}Fe_{Spl}$ (Table 2 and Fig. 3).

5. OPPOSING PREDICTIONS FOR EQUILIBRIUM IRON ISOTOPE FRACTIONATION FACTORS

As background for a discussion of the results presented above, we first review the opposing predictions for equilibrium Fe isotope fractionation between mantle minerals at high temperatures. The isotopic fractionation factor (α) between two phases is expressed in terms of the ratio of the reduced partition function ratios (β-factors). This expression can be written in the logarithmic form as:

$$\ln \alpha_{a-b} = \ln \beta_a - \ln \beta_b \tag{2}$$

where α_{a-b} is the equilibrium fractionation factor between two substances a and b, and β_a and β_b are the reduced partition function ratios for substances a and b, respectively (Urey, 1947; Bigeleisen and Mayer, 1947). Two different estimates for α_{a-b} are relevant to this study: (1) ionic-model estimates based on crystal chemical constraints, and (2) predictions from modeling Mössbauer data.

5.1. Ionic model predictions

Iron isotope fractionation is more difficult to model using density functional theory than for many other rock-forming elements because of the need to account properly for the behavior of the d electrons. While models do exist for a number of Fe-bearing materials (Blanchard et al., 2009; Rustad and Dixon, 2009), the phases of interest here have not been modeled from first principles. In lieu of such models, we consider here predictions based on an ionic approximation that is useful for gaining insights into the origins of inter-mineral fractionation.

At the most basic level, differences in vibrational frequency drive equilibrium stable isotope fractionation. Hooke's law characterizes vibrational frequencies:

$$\nu = \frac{1}{2\pi}\sqrt{\frac{K_f}{\mu}} \tag{3}$$

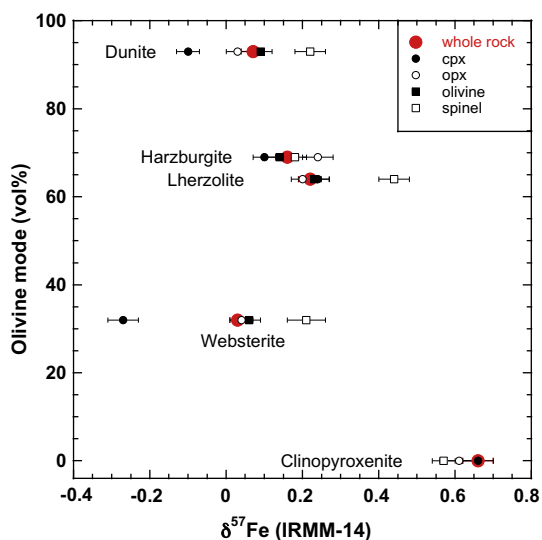where vibrational frequency, ν, depends on a force constant, K_f, which characterizes bond stiffness, and reduced

Fig. 3. $\delta^{57}Fe$ values of olivine, orthopyroxene (opx), clinopyroxene (cpx), spinel, and whole rock versus percent olivine in the corresponding xenoliths. Data from Tables 1 and 2. Error bars represent 2 standard deviations of the mean.

mass, μ. The fractionation of iron isotopes between two phases a and b (α_{a-b}) depends on the difference between the force constants for each vibrational mode for both phases as well as their masses. At high temperatures the fractionation can be approximated using an average force constant with an analytical expression (e.g., Urey, 1947; Young et al., 2002, 2009):

$$\delta^{57}Fe_a - \delta^{57}Fe_b \cong 10^3 \ln \alpha_{a-b}^{57/54}$$
$$= \frac{10^3}{24}\left(\frac{h}{k_bT}\right)^2\left(\frac{1}{m_{54}} - \frac{1}{m_{57}}\right)\left[\frac{K_{f,a}}{4\pi^2} - \frac{K_{f,b}}{4\pi^2}\right] \quad (4)$$

where m_{54} and m_{57} are the atomic masses of ^{54}Fe and ^{57}Fe respectively, k_b is Boltzmann's constant, h is Plank's constant, T is temperature in Kelvin, and $K_{f,a}$ and $K_{f,b}$ are the average force constants for phases a and b respectively. In the ionic model for inter-mineral fractionation presented by Young et al. (2009) for Mg isotope fractionation, insights into partitioning of heavy and light isotopes between minerals were gained by treating K_f in Eq. (4) as electrostatic in origin and summing over relevant and distinct bond pairs associated with the structures and compositions of the minerals in question. Here we modify the approach for Fe isotope fractionation in mantle minerals and incorporate the effect of varying the oxidation state of iron. Using this approach we can make some predictions for Fe isotope fractionation factors between phases that have broadly similar bond types, all the while acknowledging the significant limitations inherent in such calculations relative to more quantitative *ab initio* models.

The force constant for a bond between cation i (in our case Fe) and anion j (e.g., O) can be written as

$$K_{f,ij} = \frac{z_iz_je^2(1-n)}{4\pi\varepsilon_o r_{ij}^3} \quad (5)$$

where z_i and z_j are the cation and anion valences, ε_o is the electric constant (vacuum permittivity for simplicity), e is the charge of an electron, n is the exponent in the Born–Mayer formulation for ion repulsion (Born and Mayer, 1932), and r_{ij} is the equilibrium interionic distance between cation i and anion j. The equilibrium interionic distance can be calculated by adding the effective ionic radii of the cation and anion of interest from Shannon (1976) for given coordination environments and valence states. This term effectively encapsulates the concept of "mean bond strength", $\overline{s_i}$, for an ionic species i as defined by Pauling (1929):

$$\overline{s_i} = \frac{z_i}{\eta_i} \quad (6)$$

where z_i is the charge of the atom of interest, and η_i is the coordination number; charge and coordination number both effect effective ionic radii.

Eqs. (4)–(6) lead to semi-quantitative estimates of equilibrium inter-mineral fractionation of stable isotopes that can be used to predict the direction and approximate magnitude of iron isotope fractionation between coexisting minerals. Eq. (4) clearly shows that the heavy isotopes of an element tend to concentrate in substances where the element will form the stiffest (shortest, strongest) bonds. Eqs. (5) and (6) indicate that as coordination number decreases and/or oxidation state (charge) increases, bond
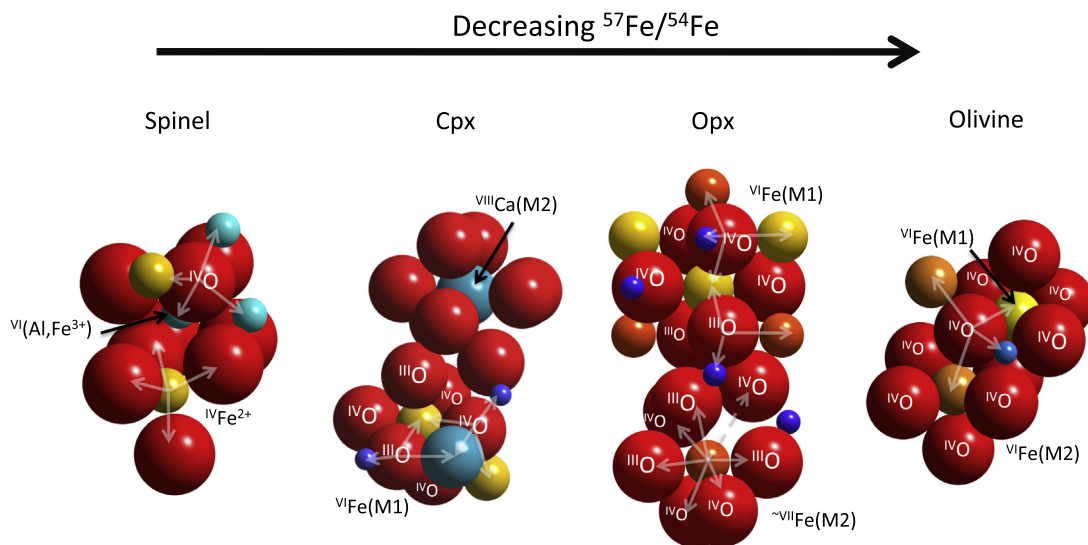

Fig. 4. Crystal structures for iron-bearing spinel, clinopyroxene (Cpx), orthopyroxene (Opx), and olivine showing nearest neighbors that influence Fe isotope fractionation. Structures are depicted using ionic radii of Shannon (1976) using CrystalMaker® software. Oxygen is shown as large red spheres in all structures. In the spinel structure, ferrous iron is shown as yellow spheres in the tetrahedrally coordinated cation site, and the blue spheres represent the octahedrally coordinated cation site that containing aluminum or ferric iron. For Cpx, iron is shown as yellow spheres occupying the octahedral M1 site, and calcium is shown as large blue spheres in the M2 site. In the Opx structure, iron is shown as yellow spheres in the octahedral M1 site, and orange spheres in the M2 site, which has an effective 7-fold coordination. The olivine structure shows octahedrally coordinated iron in both M1 and M2 crystallographic sites. Translucent arrows show examples of bonding to nearest neighbors defining the coordination spheres of interest. (For interpretation of the references to color in this figure legend, the reader is referred to the web version of this article.)

stiffness increases, leading to a shorter bond length, and in turn a larger force constant. Therefore, Eqs. (3)–(6) predict that the heavy isotopes of iron will concentrate in minerals where the iron coordination number is lowest and/or oxidation state is highest.

Based solely on the coordination environments of iron, one predicts that spinel will concentrate the heavy iron isotopes relative to olivine, orthopyroxene, and clinopyroxene. Differences in charge for iron must also be considered. Typical San Carlos spinels in this study contain primarily Fe^{2+} in tetrahedral (4-fold, $\eta_i = 4$) coordination with a small amount of Fe^{3+} in octahedral coordination (6-fold, $\eta_i = 6$) (Table 1). This is characteristic of normal spinels with the structure $^{IV}(R^{2+}_{i-1}, R^{3+}_i)^{VI}[R^{2+}_i, R^{3+}_{2-i}]$ O_4, where the inversion parameter i, characterizing deviations from the normal structure toward the inverse structure, is very much smaller than unity (Deer et al., 1992; Klein et al., 1993). The conclusion that spinel will have the highest $\delta^{57}Fe$ at equilibrium is robust with respect to the presence of the small amounts of spinel ferric iron (see below).

The fractionations involving pyroxenes are more complicated and Fig. 4 illustrates the salient features of the crystal structures that influence the equilibrium Fe isotope partitioning. Pyroxenes have the general structural formula $^{VI-VIII}M2^{VI}M1^{III-IV}O_6$, where M2 and M1 are the larger and smaller divalent/trivalent cation crystallographic sites, respectively. In general one expects higher $^{57}Fe/^{54}Fe$ for Fe^{2+} in pyroxenes relative to olivine because of the lower coordination number for some oxygens bonded to iron in pyroxenes (1/3 of M1 oxygens are ^{III}O and 3/7 of M2 oxygens are ^{III}O, Fig. 4), resulting in stiffer Fe–O bonds on average. This is the case, to first order, for Cpx where Fe occupies the octahedral M1 site (M2 is dominated by Ca) and will therefore have Fe^{2+} in 6-fold coordination only. Orthopyroxene, on the other hand, can host Fe^{2+} in the $^{VI}M1$ site and in the larger $^{VI-VIII}M2$ site; lowering the stiffness of the average Opx Fe–O bond and suggesting that orthopyroxene would have lower $^{57}Fe/^{54}Fe$ than Cpx and closer to that of Ol.

The presence of ferric iron in pyroxenes also influences the Fe isotope fractionation relative to olivine. Clinopyroxenes from our samples have $Fe^{3+}/\sum Fe$ values that range from 0.07 to 0.33, and Opx range from 0.08 to 0.15 with typical uncertainties of tens of percent of the reported values (Table 1). Ferric iron in pyroxene and its absence in olivine (within charge-balance detection limits) suggest a greater concentration of heavy iron isotopes relative to olivine than one would predict assuming pure ferrous iron in all phases. Here we assume that any ferric iron in orthopyroxene is ordered to the M1 site, and that ferrous iron is distributed across the $^{VI}M1$ and $^{VII}M2$ sites. Both Fe^{2+} and Fe^{3+} are confined to M1 in Cpx where Ca dominates the M2 site.

Qualitatively, the discussion above suggests that olivine should possess the lowest equilibrium $\delta^{57}Fe$ of all of the xenolith phases because of the combination of lower coordination environment for Fe in spinel, the lower coordination number for some oxygens in pyroxenes, and the fact that olivine is essentially free of Fe^{3+} compared with the other phases with the same Fe coordination number (i.e.,

pyroxenes) which have non-trivial amounts of ferric iron. Taking these general equilibrium fractionation rules a step further, we use Eqs. (4) and (5) to make semi-quantitative estimates of inter-mineral stable isotope fractionation among these mantle xenolith phases based on the structures and compositions of the constituent minerals. For example, using the actual mineral compositions in Table 1, we predict that the small but significant $^{VI}Fe^{3+}$ of Opx dominates over the loss of bond stiffness in the M2-site $^{VII}Fe^{2+}$ in Opx so that $\delta^{57}Fe_{Opx} > \delta^{57}Fe_{Ol}$ (Fig. 5a).

Similarly, we quantify further the spinel–olivine fractionation factor. The structural formula for an average olivine in CEM1-3, the Spl lherzolite, is $^{VI}(Mg_{1.81}Fe^{2+}_{0.18})^{IV}SiO_4$ and the average spinel has the structural formula $^{IV}(Mg_{0.73}Fe^{2+}_{0.27})^{VI}(Al_{1.19}Cr_{0.74}Fe^{3+}_{0.07})O_4$ with an average $Fe^{3+}/\sum Fe$ (Table 1) of 0.19 ± 0.09 (i.e., ~81% of its iron as $^{IV}Fe^{2+}$, and 19% as $^{VI}Fe^{3+}$). From these analyses we conclude that the San Carlos spinels have the normal spinel structure with trivalent cations in the octahedral site. Oxygen is coordinated by four cations in both olivine and spinel. Effective ionic radii indicate that the $^{VI}Fe^{2+}$–^{IV}O bond in olivine has the average bond length of $r_{Fe^{2+}[VI]-O[IV]} = 2.16 \times 10^{-10}$ m and average $^{IV}Fe^{2+}$–^{IV}O and $^{VI}Fe^{3+}$–^{IV}O bond lengths in spinel of $r_{Fe^{2+}[IV]-O[IV]} = 2.02 \times 10^{-10}$ m and $r_{Fe^{3+}[VI]-O[IV]} = 2.025 \times 10^{-10}$ m (Shannon, 1976), respectively. Calculating the average K_f using these bond lengths for the Fe–O bonds weighted by the number of bond types in the respective structures, suggests that $\delta^{57}Fe$ for spinel should be higher than that for olivine at igneous temperatures (e.g., ~0.28‰ at 800 °C, Fig. 5c).

Our results for each of the relevant fractionation factors versus temperature using the ionic model are presented in Fig. 5. Caution should be used when calculating fractionation factors with this model. As presented here, the ionic model does not take into account the potential effects of compositional variation (i.e., solid-solutions, cation substitutions) on iron isotope fractionation, which have been predicted by first principles investigations for equilibrium Ca (Feng et al., 2014) and Mg (Schauble, 2011) isotope fractionation. Nevertheless, experience shows that the calculations from our simplified ionic model do provide a method of estimating fractionation factors consistent with crystal chemical constraints to better than factors of 2 and often considerably better than that (Young et al., 2009).

The red curve in Fig. 5a (labeled Opx ionic (Fe^{3+})) represents predictions based on the ionic model made by averaging over the M1 and M2 sites, assuming the M1 site is entirely occupied by only ferric iron (the assumption is made for illustration only; it is unlikely to occur naturally). Conversely, the blue curve (labeled Opx ionic (Fe^{2+})) was calculated by averaging over the M1 and M2 sites, assuming only ferrous iron in both sites. The purple dotted curve represents ionic model predictions using the average $Fe^{3+}/\sum Fe$ (Table 1) for San Carlos Opx from this study. It is clear from Fig. 5a that if Opx contains even a small amount of ferric iron in the M1 site, Opx will concentrate the heavy isotopes of iron relative to Ol, as suggested qualitatively above, but the magnitude of the fractionation will be small.
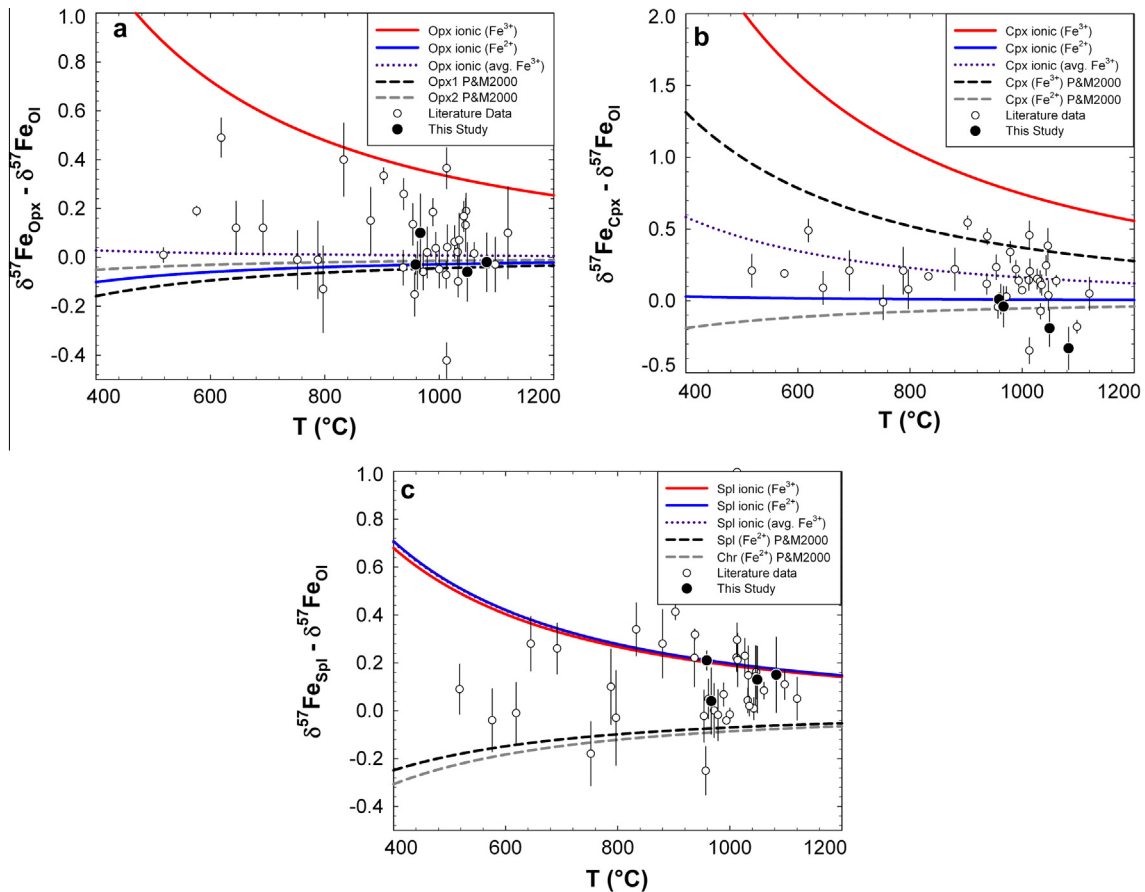
Fig. 5. Plots showing the calculated temperature dependence of (a) $\delta^{57}Fe_{Opx}$–$\delta^{57}Fe_{Ol}$, (b) $\delta^{57}Fe_{Cpx}$–$\delta^{57}Fe_{Ol}$, and (c) $\delta^{57}Fe_{Spl}$–$\delta^{57}Fe_{Ol}$ using the ionic model (this study) and modeling of Mössbauer data from Polyakov and Mineev (2000). Red and blue solid curves and purple dotted curves were calculated using ionic model assuming all ferric iron in the relevant crystallographic site, all ferrous iron in the site, and the average $Fe^{3+}/\sum Fe$ content of minerals from this study, respectively (solid blue and purple dotted curves overlap in (c)). Black and gray dashed lines represent modeling of Mössbauer data for two different Opx compositions (a), one Cpx composition with two different valence states of iron (b), and two different Spl compositions (c). Small open symbols represent data from mantle xenoliths from Williams et al. (2005), Zhao et al. (2010), and Zhao et al. (2012); larger closed symbols represent data from this study. Error bars are 2 standard deviation uncertainties. Temperatures for the xenoliths from this study were calculated using the Ol–Spl geothermometer of Wan et al. (2008); those of Zhao et al. (2010, 2012) were calculated using the Spl–Opx–Ol geothermometer of Sachtleben and Seck (1981); and those from Williams et al. (2005) were calculated with the Ol–Spl thermometer of Ballhaus et al. (1991). See text for further discussion. (For interpretation of the references to color in this figure legend, the reader is referred to the web version of this article.)

Similarly, for Cpx–Ol fractionation predictions based on the ionic model (Fig. 5b), the red curve represents purely Fe^{3+} in the M1 site of Cpx, the blue curve represents purely Fe^{2+} in the site, and the purple dotted curve is representative of the average ferric/ferrous content of Cpx in our samples. For Spl–Ol fractionation predictions (Fig. 5c), the red curve is based on the ionic model assuming all ferric iron in the octahedral cation site, while the blue curve assumes all ferrous iron in the tetrahedral cation site. Again, the purple dotted curve represents the average $Fe^{3+}/\sum Fe$ of Spl from this study. The ionic model predicts that both Cpx and Spl will concentrate the heavy isotopes of iron relative to Ol, no matter the ferric iron content of the minerals.

The predicted order of fractionation for the average mineral compositions in San Carlos xenoliths according to the ionic model is $\delta^{57}Fe_{Spl} > \delta^{57}Fe_{Cpx} > \delta^{57}Fe_{Opx} >$

$\delta^{57}Fe_{Ol}$. As previously mentioned, in every rock presented here, $\delta^{57}Fe_{Spl} > \delta^{57}Fe_{Ol}$, which is in agreement with crystal chemical expectations, whereas clinopyroxene iron isotope data in these xenoliths appear erratic, following no clear, systematic trend (Fig 5). See the Electronic Annex (Appendix B) for an interactive spreadsheet that includes all ionic model calculations shown in Fig. 5.

5.2. Mössbauer predictions

Iron isotope fractionation between minerals can also be predicted by modeling Mössbauer second-order Doppler shift data to arrive at partition function ratios. Using this approach, Polyakov (1997) and Polyakov and Mineev (2000) predict that spinel will concentrate the light iron isotopes relative to olivine, a trend that is opposite to expecta-

tions from crystal chemical considerations and the predictions from the ionic model described in the previous section. In order to determine the affinity of Fe isotopes for a given phase from Mössbauer data, one must relate the kinetic energy for the phase indicated by the thermal shift (second-order Doppler shift) of the recoil-free Mössbauer resonant frequency to partition function ratio with the expression:

$$\ln \beta = \frac{\Delta m}{\bar{m}} \left(\frac{-Smc}{RT} - \frac{3}{2} \right) \qquad (7)$$

where S is the Mössbauer second-order Doppler shift (m/s), m is mass, other symbols have their usual meanings, and the product Smc is kinetic energy. Combining Eqs. (7) and (2) one can predict the resulting fractionation factors between certain minerals and olivine as a function of temperature.

Fig. 5a shows the Opx–Ol fractionation versus temperature for Mössbauer data from two different Fe^{2+}-bearing orthopyroxenes compared with the predictions from crystal chemical constraints. The results of the two prediction methods for ferrous iron generally agree in predicting a slightly negative Opx–Ol fractionation at equilibrium (i.e., $\delta^{57}Fe$ Opx $< \delta^{57}Fe$ Ol). The dashed black curve labeled Opx1 P&M2000, represents an enstatite with the formula $Mg_{1.95}Fe_{0.05}Al_{0.05}Si_{1.96}O_6$, while the dashed gray curve labeled Opx2 P&M2000, represents an enstatite with the formula $Mg_{1.65}Fe_{0.27}Al_{0.03}Si_{2.03}O_6$ (Polyakov and Mineev, 2000). Both Opx phases have iron present as Fe^{2+} only and can be compared with the Fe^{2+} ionic model predictions. Note that the prediction from Mössbauer data for the more iron rich orthopyroxene (Opx2 P&M2000; dashed gray curve) is slightly greater than that based on the ionic model assuming all Fe is Fe^{2+} (blue curve). The less iron rich orthopyroxene (Opx1 P&M2000; dashed black line) from Polyakov and Mineev (2000) suggests a more negative Opx–Ol fractionation, though the differences are extremely small (of order 0.02 per mil) at relevant temperatures.

The predicted Cpx–Ol fractionation with temperature based on Mössbauer data from a Cpx with composition $Ca_{1.16}Mg_{0.64}Fe_{0.31}Si_{1.94}O_6$ is compared with the prediction from this study in Fig. 5b. The agreement is reasonable (factor of $\sim$2) at comparable iron charge states. The dashed gray curve represents modeling Mössbauer data for ferrous iron in the M1 site of Cpx, while the dashed black curve is for ferric iron. These curves should be comparable to the corresponding curves based on the ionic model shown as solid blue and red, respectively. There is rough agreement between the Mössbauer data and ionic estimates as to the effects of ferric iron substitution (Fig. 5b), and the positive Cpx–Ol fractionation predicted here for the average ferric iron content of the San Carlos xenoliths Cpx lies midway between the Fe^{2+} and Fe^{3+} estimates from the Mössbauer data.

While there is general agreement between signs and relative magnitudes of Fe^{2+} and Fe^{3+} isotope fractionation among Opx, Cpx, and Ol based on Mössbauer data and the ionic crystal chemical model, the predictions for Spl–Ol fractionation do not agree. Fig. 5c shows the Spl–Ol fractionation predictions from Mössbauer data for two different spinel compositions: magnesium spinel, $Mg_{0.9}Fe_{0.1}$

Al_2O_4 (dashed black curve labeled Spl (Fe^{2+}) P&M2000), and Ferrochromite, $FeCr_2O_4$ (dashed gray curve labeled Chr (Fe^{2+}) P&M2000). Both compositions show Spl–Ol fractionation opposite in sign to predictions based on the ionic model (solid red, solid blue, and dotted purple curves). In other words, predictions of equilibrium iron isotope fractionation based on modeling Mössbauer data are antithetic to the predictions based on expectations from consideration of charge and coordination number discussed in Section 5.1.

Should we believe the crystal chemical constraints? Comparisons between data and expectations in other instances may help answer this question. For example, the large shift in coordination between spinel and olivine, from 4-fold to 6-fold, is analogous to the difference in coordination environment between garnet, where Fe^{2+} exists in 8-fold coordination, and olivine where it is in 6-fold coordination. Williams et al. (2009) report a 0.4 per mil difference in $^{57}Fe/^{54}Fe$ between Cpx and garnet (Grt) at $\sim$1450 K in eclogites ($\delta^{57}Fe$ Cpx $> \delta^{57}Fe$ Grt by 0.4 per mil). The ionic model embodied by Eqs. (4)–(6) predicts 0.39 per mil at this same temperature. We take this as evidence that large differences in coordination number should be good guides for relative isotope fractionation.

Although existing data from mantle rocks give inconsistent clues to equilibrium fractionation factors in detail, it is nonetheless useful to compare these results in aggregate with the predicted fractionation factors as functions of temperature in Fig. 5. For this purpose we use temperature estimates from cation thermometry (Ballhaus et al., 1991; Sachtleben and Seck, 1981; Wan et al., 2008), recognizing that isotope fractionation and cation partitioning may not record precisely the same temperatures. We note that although the scatter is well beyond analytical uncertainties, regardless of the temperature estimates, and many stark exceptions exist, the preponderance of the data suggest $\delta^{57}Fe_{Spl} > \delta^{57}Fe_{Ol}$, $\delta^{57}Fe_{Cpx} > \delta^{57}Fe_{Ol}$, and $\delta^{57}Fe_{Opx} \sim \delta^{57}Fe_{Ol}$, consistent with expectations from crystal chemistry for equilibrium inter-mineral isotope fractionation.

6. DISCUSSION

6.1. Inter-mineral fractionation and open system processes

Having established reasonable models for equilibrium Fe isotope fractionation between the major mantle minerals that are at least robust with respect to sign if not exact magnitude, we now are in position to investigate departures from equilibrium. Here we compare our data for the inter-mineral fractionations in five San Carlos xenoliths with previously published models and the expectations from Eqs. (4)–(6) to better understand the systematics of iron isotope partitioning between mantle minerals. Our data show variation in the Fe isotope compositions of minerals in a single xenolith and variation between individual xenoliths (whole-rock values) from San Carlos, AZ (Table 2 and Fig. 3). We first address whether Fe isotope equilibrium has been achieved among minerals within our samples.

Plots of the isotope compositions of mineral pairs are good indicators of stable isotope equilibration (so-called
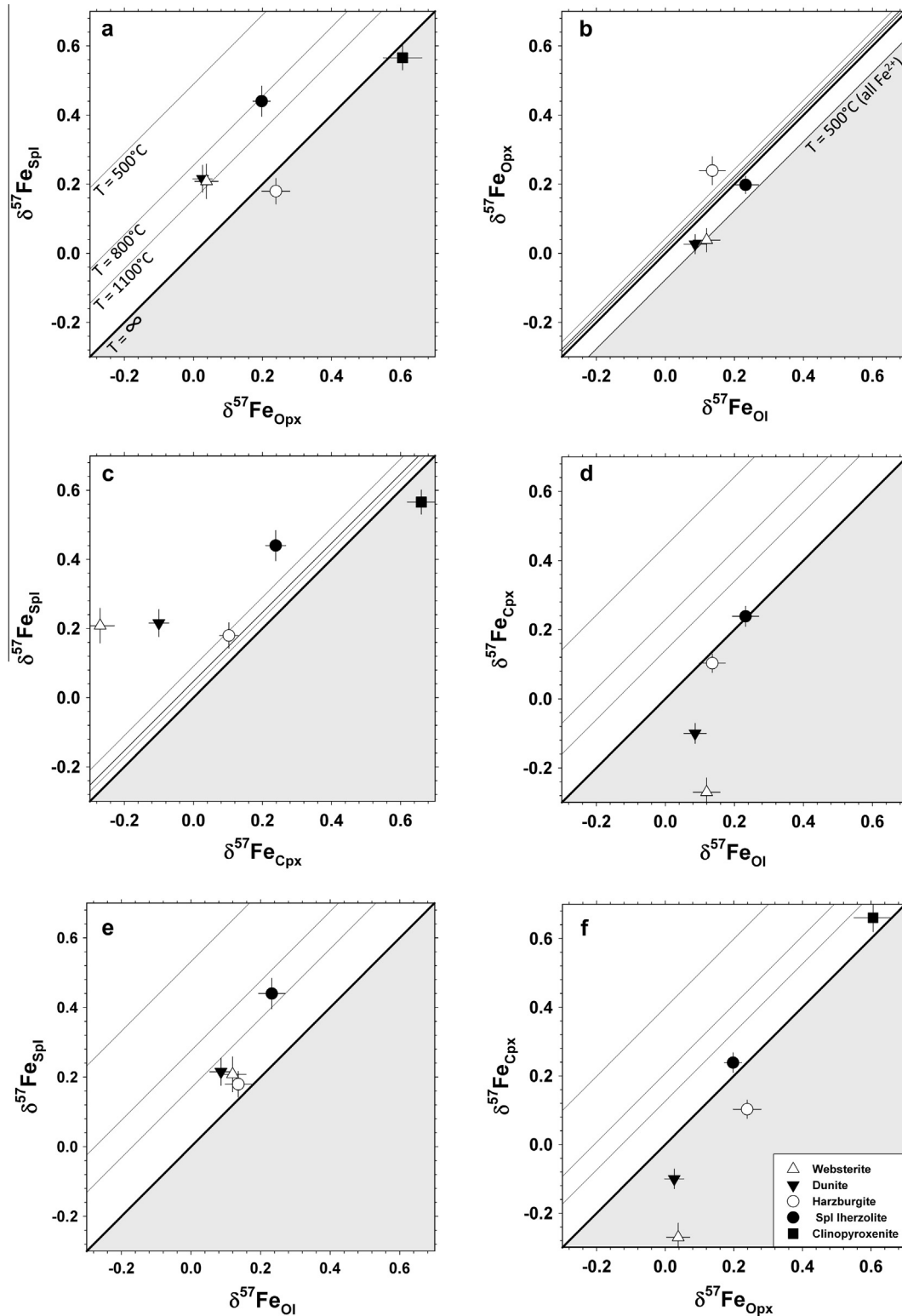
Fig. 6. Fe isotope fractionation between minerals in San Carlos mantle xenoliths. Heavy solid lines represent $T = \infty$. Thin lines represent equilibrium fractionation calculations using the ionic model for average mineral compositions at $T = 500$, 800, and 1100 °C. Gray shaded regions indicate disequilibrium. See text for further explanation. Error bars on individual data points depict 2 standard deviations of the mean (Table 2).

"$\delta-\delta$" plots; e.g., Gregory and Criss, 1986). Mineral pairs plotting on a line with slope of ~1 on a plot of δ_a vs. δ_b plot for phases a and b, are thought to be in equilibrium with each other. This can be seen with reference to the definition of the fractionation factor expressed in terms of delta values: $\alpha_{a-b} = (10^3 + \delta_a)/(10^3 + \delta_b)$. This equation can be rearranged to yield $\delta_a = (\alpha_{a-b})(\delta_b) + 10^3(\alpha_{a-b} - 1)$. Since α_{a-b} is close to unity (e.g., 1.00×), isotherms in plots of δ_a vs. δ_b have slopes of unity with intercepts determined by the temperature (because $10^3(\alpha_{a-b} - 1)$ is the temperature-dependent fractionation between phases a and b in delta notation). What is more, regardless of the number of phases hosting the element of interest, data falling below the line with a zero intercept, corresponding to infinite temperature (i.e., $\alpha_{a-b} = 1$), signify open-system isotope exchange (Gregory and Criss, 1986). Violation of the sign of the equilibrium fractionation then becomes a tell-tale sign of disequilibrium, regardless of the exact magnitude of the expected equilibrium partitioning.

Fig. 6a–f are $\delta^{57}Fe_a$–$\delta^{57}Fe_b$ plots of every possible mineral pair a and b present in the xenoliths measured for this study. The heavy solid line on each plot is $\delta^{57}Fe_a = \delta^{57}Fe_b$, and represents equilibration of the minerals at $T = \infty$. The light solid lines were calculated using the ionic model at $T = 500$, 800, and 1100 °C (labeled in a) using the average $Fe^{3+}/\sum Fe$ of minerals from this study (as in the purple dotted curves in Fig. 5). The additional isotherm on Fig. 6b (on the opposite side of the $T = \infty$ line) represents the fractionation based on the ionic model at $T = 500$ °C, but assuming no ferric iron present in the Opx M1 crystallographic site. Mineral pairs plotting in the gray shaded areas on all plots in Fig. 6 are regarded as exhibiting clear signs of inter-mineral isotopic disequilibrium. Given the high temperatures involved, this disequilibrium is likely due to open-system isotope exchange (such as metasomatic alteration). The mineral pairs that have undergone open-system processes need not follow any obvious pattern for degree of enrichment of $^{57}Fe/^{54}Fe$. Instead, the patterns will depend on the metasomatic history of the sample and the susceptibility of each phase to exchange. Similar plots have been used to investigate the oxygen isotope systematics of mantle xenoliths, leading to the conclusion that metasomatism preferentially affects the oxygen isotope signals of pyroxenes relative to olivine and spinel from mantle samples (e.g., Mattey et al., 1994; Perkins et al., 2006).

Fig. 6a–d and f show $\delta^{57}Fe$ vs. $\delta^{57}Fe$ plots involving one or more pyroxene. In each case there is the suggestion of disequilibrium due to open-system processes evidenced by violations of the sign expected for equilibrium fractionation (although in the case of the small fractionation between Opx and Ol the sign depends critically on the Fe^{3+} content of the Opx). The evidence for disequilibrium is unequivocal in the case of Cpx where the case for disequilibrium is independent of the details of the estimates of ferric iron content. For example, referring to Fig. 5b, the Cpx–Ol data for the Spl lherzolite and the harzburgite could be taken as being consistent with predictions, albeit only with the assumption of $Fe^{2+} = \sum Fe$, while the dunite and websterite are clearly reversed in sign compared with either the ionic model or the predictions from Mössbauer data regardless of the charge

state of the Fe. This is made clear in Fig. 6d in which the Cpx–Ol pairs for the dunite and websterite lie well within the disequilibrium portion of the plot. This conclusion is supported by a similar study on magnesium isotopes by Young et al. (2009) in which pyroxenes in two San Carlos xenoliths (one of them being CEM1-3 from this study), were shown to be out of magnesium isotopic equilibrium, and did not agree with fractionation estimates based on density functional theory calculations (Schauble, 2011).

Because in all samples measured here, $\delta^{57}Fe$ of spinel is greater than $\delta^{57}Fe$ of olivine, these data are consistent with expectations based on coordination and valence state of iron as described in the ionic model, but inconsistent with the predictions made by modeling Mössbauer data. The fact that spinels have higher $^{57}Fe/^{54}Fe$ than the coexisting olivine in these rocks is understood as purely a coordination effect rather than an oxidation state effect; as mentioned earlier, our spinel samples are calculated to have small amounts of octahedrally coordinated Fe^{3+} in their structures, with most of the iron existing as Fe^{2+} in the tetrahedral site. Similar influence of coordination was seen for Mg isotope partitioning between spinel and olivine (Young et al., 2009). This is an important observation as it has been suggested that oxidation state is the primary control on Fe isotope fractionation. For example, Williams et al. (2004, 2005) described the considerable iron isotope variation in mantle spinels as reflecting mantle redox processes. Plots of $\delta^{57}Fe$ and $Fe^{3+}/\sum Fe$ of San Carlos spinels show no clear correlation (Fig. 7). It seems that in the case of spinel, coordination environment is the major determinant of inter-mineral Fe isotope fractionation. Iron isotope data from Zhao et al. (2010) also support this hypothesis, indicating that oxygen fugacity may not be the main control on iron isotope fractionation in spinels in the mantle. Indeed, our calculations shown in Fig. 5c suggest that iron oxidation state is subordinate to the effect of tetrahedral coordination; the curve representing tetrahedrally coordinated ferrous iron (blue curve) is only slightly greater than the one representing octahedrally coordinated ferric iron (red curve).
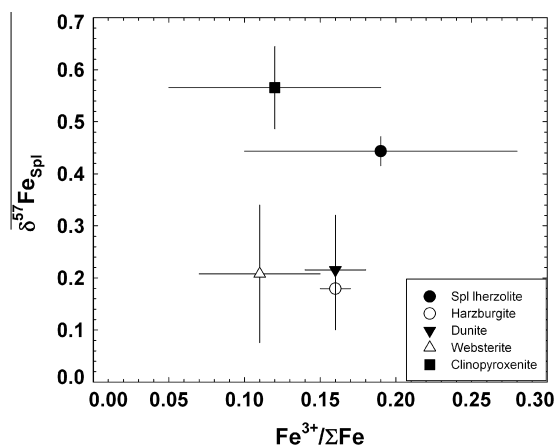

Fig. 7. Spinel $\delta^{57}Fe$ values versus $Fe^{3+}/\sum Fe$ in San Carlos xenoliths. Data from Tables 1 and 2. Error bars are 2 standard deviations.

In view of the strong influence of tetrahedral coordination on Mg isotope fractionation involving spinel (Young et al., 2009), and because of the similarly large positive Spl–Ol fractionation prediction shown in Fig. 5c, we can find no compelling evidence that the expectation that tetrahedral coordination of Fe in spinel should *not* lead to δ^{57}Fe Spl > δ^{57}Fe Ol $\sim \delta^{57}$Fe Opx at equilibrium. Therefore, in Fig. 6a and e, where we have used the ionic model prediction for the equilibrium fractionation factors, the data are consistent with Spl, Ol, and possibly Opx being in, or approaching, isotopic equilibrium.

6.2. Fe isotopes and petrologic processes in subcontinental mantle lithosphere

6.2.1. Partial melting

Olivine-rich Group I xenoliths have been widely interpreted as partial melting residues with the lherzolites considered closest to primitive mantle material capable of generating a basaltic magma (Frey and Prinz, 1978; Galer and O'Nions, 1988). Frey and Prinz (1978) noted strong trends in bulk chemical composition (major elements), mineral composition, and modal proportion in San Carlos xenoliths. They determined that whole-rock major-element compositional trends are not caused by varying proportions of minerals with identical major element compositions. These trends are instead the result of systematic mineral compositional changes that accompany the modal changes. The combination of these two effects together causes the variations seen in bulk chemical compositions of San Carlos xenoliths.

As illustrated in Fig. 3, similar trends are seen in Fe isotope composition in the Group I xenoliths from this study (i.e., neglecting the transitional websterite sample). The whole-rock δ^{57}Fe of Group I xenoliths decreases with increasing olivine content. To first order, this observation is consistent with the idea that olivine-rich Group I xenoliths are the residues of partial melting episodes. The order of mineral consumption upon partial melting is Cpx, then Opx, then Spl, and finally Ol (e.g., Jaques and Green, 1980; Takahashi and Kushiro, 1983; Walter and Presnall, 1994). According to the ionic model presented in Section 5.1, the order of degree of enrichment of the heavy isotopes of iron in typical mantle xenoliths is δ^{57}Fe$_{Ol}$ < δ^{57}Fe$_{Opx}$ < δ^{57}Fe$_{Cpx}$ < δ^{57}Fe$_{Spl}$. If a fertile lherzolite with typical upper-mantle Fe isotope ratios is partially melted and the melt is extracted, the resulting residues will contain less Cpx and Opx. If no exchange of iron isotopes occurs between the residual olivine-rich solids and the extracted melt, the preferential loss of those phases that concentrate the heavy iron isotopes will lead to light isotope enrichment in the residue. However, this behavior alone cannot account for the full range of whole rock Fe isotope compositions seen in our olivine-rich Group I samples (lherzolite, harzburgite, and dunite) because the fractionation between olivine and pyroxenes is too small.

Several studies have suggested redox-controlled iron isotope fractionation during melting as the process responsible for observed whole rock ^{57}Fe/^{54}Fe variations (e.g., Williams et al., 2005; Dauphas et al., 2009). These studies

explored the possibility that equilibrium fractionation between Fe^{2+} and Fe^{3+} (the latter forming stiffer bonds) during mantle melting could be the primary control on the iron isotopic variations among mantle xenoliths. Fe^{3+} is approximately ten times more incompatible than Fe^{2+} during mantle melting according to some studies (Canil et al., 1994; Woodland et al., 2006). The average coordination of Fe^{2+} and Fe^{3+} is approximately 5 in basaltic melts (e.g., Jackson et al., 2005; Wilke et al., 2005), while it is ~ 6 in Cpx, Opx, and Ol. The lower coordination numbers in melts apply to both ferrous and ferric iron, suggesting that even in the absence of differences in oxidation state, there is a tendency for melts to concentrate the heavy isotopes of Fe. Therefore, on the basis of coordination change and partitioning of ferrous and ferric iron during melting, one expects melts to favor the heavy iron isotopes relative to the resulting residue.

Dauphas et al. (2009) introduced a quantitative model relating the iron isotopic composition of magmas to the degree of partial melting, Fe^{2+} and Fe^{3+} concentrations, and the oxidation state buffering capacity of the mantle. The model attributes the fractionation of Fe isotopes to the difference in Fe oxidation state only. Experiments by Schuessler et al. (2007) in which the Fe fractionation between pyrrhotite and a peralkaline rhyolitic melt was measured showed a fractionation of approximately +0.35‰ at temperatures ranging from 840 to 1000 °C. Dauphas et al. (2009) estimated the fractionation factor for pyrrhotite-melt and combined it with the β-factor for pyrrhotite derived by Polyakov et al. (2007) to assign a β-factor to silicate melt (which is the average contribution from 62% ferric and 38% ferrous iron in this case) by difference. Then, assuming that Fe^{2+} in melts has the same β-factor as Fe^{2+} in silicates, they derive the β-factor for Fe^{3+} in a peralkaline rhyolitic melt, which corresponds to a fractionation factor between Fe^{2+} and Fe^{3+} of $\sim +0.3$‰ in the melt.

Dauphas et al. (2009) point out the limitations of the assumptions in their model, noting that the differences in iron coordination environments in solids and melts may enhance the isotopic fractionation during mantle melting. One can use Eqs. (4) and (5) to crudely estimate that a ^{57}Fe/^{54}Fe fractionation of ~ 0.02‰ might exist between olivine and melt at 1200 °C based solely on the difference between 6 and 5-fold coordination of Fe between olivine and melt, respectively. This fractionation can be compared with the value of ~ 0.17‰ for melt/solid Fe isotope fractionation derived by Dauphas et al. (2009) if we assume a single step of equilibrium melting, an intra-melt ^{57}Fe/^{54}Fe fractionation factor of 0.44‰ (their estimated value), and a Fe^{3+}/Fe^{2+} 10 times that of the source rock (i.e., a melt Fe^{3+}/Fe^{2+} of ~ 0.4 based on their estimated liquid/solid distribution coefficient for Fe^{3+} being 10 times that of Fe^{2+} and source rock Fe^{3+}/Fe^{2+} of about 0.04).

For the moment we use the Dauphas et al. (2009) model recognizing that there is room for amendment. The solid line in Fig. 8 represents evolution of a solid residue from extracted melt, calculated using equations for "buffered" fractional melting model of Dauphas et al. (2009) their Appendix B. By "buffered" the authors refer to a fixed
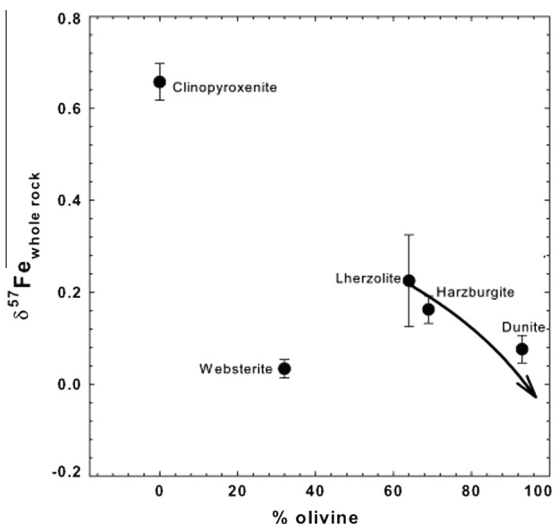
Fig. 8. Whole-rock δ^{57}Fe values versus percent olivine in the corresponding xenoliths; data from Tables 1 and 2. The solid curve represents the path of a partial melting residue and was calculated using the model for Fe isotope fractionation during partial melting from Dauphas et al. (2009). See main text for details. Error bars on all data points (except for the lherzolite) depict 2 standard error and are calculated by regressing the errors of constituent mineral δ^{57}Fe values. Error bars on the lherzolite represent 2 standard error as determined by direct measurement of the powdered rock by MC-ICPMS (Table 2).

$(Fe^{3+}/Fe^{2+})_{liquid}/(Fe^{3+}/Fe^{2+})_{solid}$, and not fixed oxygen fugacity in their calculations. We modified the model by using bulk Fe^{3+}/Fe^{2+} and δ^{57}Fe values of CEM1-3 (our spinel lherzolite) as the fertile source rock (initial composition of the residue). Also, in order to plot the curves on Fig. 8, we convert degree of partial melting (%) to modal% olivine. This was achieved by interpolating data from melting experiments of Kinzler (1997) relating mineral mode in a partial melting residue to the degree of partial melting. This approach is a simplification in that, in addition to partial melting extent, the olivine modal abundance may also be controlled by interaction with passing, channelized olivine-saturated melts (Kelemen et al., 1995). Nonetheless, for our purposes, the essential feature of the calculation is the degree of liquid–solid exchange. The resulting curve in Fig. 8 suggests that the bulk iron isotope values of the lherzolite, harzburgite, and dunite of this study are consistent with fractionation by liquid-solid exchange during partial melting, as modeled here, or by other mechanisms, assuming a fixed Fe^{3+}/Fe^{2+} in the phases during exchange and that the fractionation factor is dominated by Fe^{3+}/Fe^{2+}. Contributions from the differences between coordination environments of Fe in silicates (~6) and melt (~5) are not represented in calculations here, but would serve to enhance the degree of fractionation to some extent.

Dauphas et al. (2009) notes that the chemical agent that would be responsible for fixing the Fe^{3+}/Fe^{2+} in their model is uncertain (it must be something other than oxygen). The model invokes constant values for $K = [Fe^{2+}]_{liquid}/[Fe^{2+}]_{solid}$, $(Fe^{3+}/Fe^{2+})_{liquid}/(Fe^{3+}/Fe^{2+})_{solid}$, and $\Delta = (\alpha - 1)10^3$. However, these approximations become problematic at high degrees of partial melting. We used pMELTS (Ghiorso et al., 2002) to track the ferric/ferrous ratio of liquid during fractional partial melting (Fig. 9). We find that at fixed oxygen fugacity of QFM-1 (a reasonable approximation), $(Fe^{3+}/Fe^{2+})_{liquid}/(Fe^{3+}/Fe^{2+})_{solid}$ is much lower than 10 and far from constant (Fig. 9a). Fig. 9b illustrates the change in δ^{57}Fe of the solid residue depending on the value one uses for a constant $(Fe^{3+}/Fe^{2+})_{liquid}/(Fe^{3+}/Fe^{2+})_{solid}$ in the "buffered" fractional melting model of Dauphas et al. (2009). Also shown is the effect of changing the fractionation factor, represented by Δ. As melting proceeds, $(Fe^{3+}/Fe^{2+})_{liquid}/(Fe^{3+}/Fe^{2+})_{solid}$ rises profoundly (Fig. 9a), suggesting a steeper negative
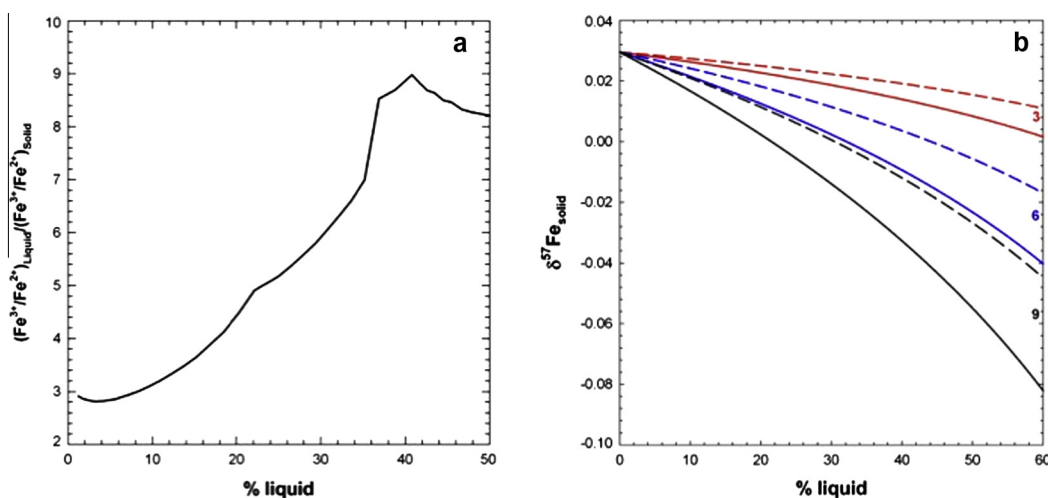
Fig. 9. Changes in $(Fe^{3+}/Fe^{2+})_{liquid}/(Fe^{3+}/Fe^{2+})_{solid}$ (a), and associated iron isotope ratios of the solid residue (b), for various constant values $(Fe^{3+}/Fe^{2+})_{liquid}/(Fe^{3+}/Fe^{2+})_{solid}$, as a function of melt extracted. Solid lines in (b) were calculated using $\Delta = 0.3‰$, while dashed lines represent $\Delta = 0.2‰$. Red lines, $(Fe^{3+}/Fe^{2+})_{liquid}/(Fe^{3+}/Fe^{2+})_{solid} = 3$; blue lines, $(Fe^{3+}/Fe^{2+})_{liquid}/(Fe^{3+}/Fe^{2+})_{solid} = 6$; black lines, $(Fe^{3+}/Fe^{2+})_{liquid}/(Fe^{3+}/Fe^{2+})_{solid} = 9$. Calculations were made using the pMELTS software (Ghiorso et al., 2002). (For interpretation of the references to color in this figure legend, the reader is referred to the web version of this article.)

slope relating fractionation and percent melting; actual melting paths would cross $(Fe^{3+}/Fe^{2+})_{liquid}/(Fe^{3+}/Fe^{2+})_{solid}$ isopleths in Fig. 9b with steeper negative slopes, as indicated by the variations in $(Fe^{3+}/Fe^{2+})_{liquid}/(Fe^{3+}/Fe^{2+})_{solid}$ in Fig. 9a. However, in all cases, the implied extent of light isotope enrichment in the solid residue is considerably less than that obtained using a fixed $(Fe^{3+}/Fe^{2+})_{liquid}/(Fe^{3+}/Fe^{2+})_{solid}$ of 10. Based on these calculations, it seems that the "buffered" (i.e., fixed Fe^{3+}/Fe^{2+}) fractional melting model of Dauphas et al. (2009) should significantly overestimate the changes in $\delta^{57}Fe$ with modal olivine where the latter is a proxy for fraction of melt extracted. Still, their model fits our data (Fig. 8).

The high $\delta^{57}Fe$ value of the clinopyroxenite compared with the other Group I peridotites can be explained by its independent origin. Frey and Prinz (1978) concluded that the Cpx-rich Group I xenoliths formed as a result of cumulate processes involving a magma (unrelated to the host basanite) interacting with and altering the Ol-rich Group I rocks in the lithosphere as it ascends, and subsequently forming cumulates that precipitate along the edges of feeder dikes. This process can explain the high $\delta^{57}Fe$ value of the clinopyroxenite and its linear correlation with the other Group I xenoliths (Fig. 8). As the rising magma percolates through the overlying lithosphere it will react with the minerals it contacts along grain boundaries, preferentially leaching the heavy iron isotopes into the melt. Formation of cumulates from such an enriched magma will have higher $^{57}Fe/^{54}Fe$ values than the partial melting residues it passed through during ascent, but will be petrogenetically linked to those residues due to the high temperature interaction/alteration (Fig. 8). This interpretation is in agreement with those of Williams and Bizimis (2014) about the origin of relatively heavy Fe isotope values in Hawaiian pyroxenites versus peridotites, which they also attribute to fractional crystallization and cumulate forming processes near the base of the oceanic lithosphere.

6.2.2. Metasomatic alteration

San Carlos Group I xenoliths are variably affected by later metasomatism by magmas or fluids (e.g., Frey and Green, 1974; Frey and Prinz, 1978; Menzies, 2003). Evidence for later modification of Group I rocks includes LREE enrichment (Frey and Green, 1974). The primary host for LREE is clinopyroxene and to a lesser extent orthopyroxene, so the pyroxenes are interpreted to have been the most strongly affected by metasomatism. Kyser (1990) found that $\delta^{18}O$ of San Carlos Opx and Cpx were similar, but they were not in equilibrium with olivine. Huang et al. (2010) and Feng et al. (2014) determined that Ca isotope measurements in Opx and Cpx from mantle samples were in equilibrium with each other, but they did not measure co-existing Ol or Spl. Jeffcoate et al. (2007) reported Li isotopic disequilibrium in pyroxenes (especially Cpx) from San Carlos xenoliths, which they attributed to exchange with young interstitial melts. Young et al. (2009) demonstrated that San Carlos pyroxenes have been shifted out of magnesium isotope equilibrium. They measured the Mg isotope compositions of minerals and whole-rocks for two San Carlos xenoliths, a spinel lherzo-lite (the same sample measured here for Fe isotopes) and a spinel harzburgite. In both rocks, the $\delta^{26}Mg$ values indicated that pyroxenes were out of equilibrium with spinel and olivine, which Young et al. (2009) reasoned was caused by metasomatism or late-stage exchange with a proximal melt.

Our study reveals that San Carlos clinopyroxenes (and in some cases, orthopyroxenes) also appear to be out of Fe isotope equilibrium with olivine and spinel, which appear to always be in equilibrium with each other. Evidently, the metasomatic process that led to LREE enrichment and O, Li and Mg isotope disequilibrium also affects the Fe isotope systematics. Because the pyroxenes are of relatively low abundance in most samples, their disequilibrium Fe isotope compositions impart minimal influence on the bulk rock compositions (exceptions being the clinopyroxenite and websterite). Accordingly, it is unlikely that the metasomatic events they record account for the wide range of whole rock $^{57}Fe/^{54}Fe$ in mantle xenoliths from different geodynamic settings (Fig. 1; cf., Poitrasson et al., 2013). As illustrated in Fig. 6, Opx and Cpx are typically lighter than expected for equilibrium with spinel. The metasomatic agent responsible for modifying their Fe isotope compositions should cause lower $^{57}Fe/^{54}Fe$ ratios in pyroxenes. Such an agent cannot be a magma derived by partial melting of the San Carlos Group I peridotites, as this magma will have higher $^{57}Fe/^{54}Fe$.

Several lines of evidence indicate that magmas or fluids more readily alter pyroxenes than olivine and spinel at mantle conditions. Clinopyroxene and orthopyroxene are less refractory than olivine and spinel during mantle melting according to thermodynamic calculations and experiments (e.g., Takahashi and Kushiro, 1983; Walter and Presnall, 1994). Gudfinnsson and Presnall (2000) found that Fe–Mg exchange coefficients (K_{dFe-Mg}^{xl-liq}) for olivine and spinel are virtually independent of temperature and pressure, whereas the coefficients for the pyroxenes increase with temperature and pressure, with clinopyroxene showing the most variation. Experiments done at upper mantle $P–T$ conditions also find pyroxenes are more soluble in high $P–T$ aqueous solutions than olivine (e.g., Macris and Manning, 2006; Newton and Manning, 2006; Wykes et al., 2011). Thus, regardless of whether the metasomatic agent is a magma, a fluid, or an intermediate phase, it is sensible that clinopyroxene, and to a lesser degree, orthopyroxene are the minerals most modified in the lithospheric mantle in terms of major oxides and isotopic compositions.

The Fe isotope composition of the olivine websterite and its constituent minerals likely reflects a more complex metasomatic history. The spinel and pyroxene compositions (Fig. 2) suggest that this xenolith is transitional between Groups I and II. This could imply a Group I protolith that is strongly modified by the host basanite magma or associated fluids. The Cpx in this sample has the lowest $\delta^{57}Fe$ value determined in this study (−0.27‰), and it exhibits the greatest degree of disequilibrium from coexisting olivine and spinel. This may suggest that an already metasomatized Group I was subsequently modified again during entrainment in the host magma.

Our results show that δ^{57}Fe values of whole rocks and individual minerals vary considerably in the San Carlos xenolith suite (Table 2, Fig. 3). As demonstrated above, these variations can be tied to petrologic processes in the subcontinental mantle lithosphere, including partial melting and metasomatism by magmas and/or fluids. Although further work on larger sample suites will surely refine these interpretations, an important outcome of this study is that comparisons of isotopic ratios within or between individual sample suites, as in Fig. 1, can be highly misleading in the absence of supporting petrologic context.

7. CONCLUSIONS

The main conclusions to be drawn from this study are:

1. Our data are consistent with the Fe isotope data of mantle xenoliths reported in previous studies in that they all show Fe isotope variations between minerals within a single sample and between mantle xenoliths, suggesting a locally heterogeneous Fe isotope composition for the lithospheric mantle.
2. $\delta-\delta$ plots of San Carlos xenolith minerals suggest that spinel, olivine, and possibly orthopyroxene are in isotopic equilibrium, but clinopyroxene appears to have been affected by some open system processes. This apparent disequilibrium involving clinopyroxene can be attributed to late stage metasomatism, perhaps interaction with a migrating melt.
3. Comparisons of Fe isotope fractionations between spinel and olivine in individual San Carlos xenoliths agree generally with the sign and order of Fe equilibrium intermineral fractionation predicted by consideration of charge and coordination (an ionic crystal chemical approximation), but disagree with the sign and order of fractionation predicted by modeling Mössbauer data.
4. Coordination environment plays the major role in equilibrium inter-mineral iron isotope fractionation between spinel and olivine in the mantle, with modulation by variable $Fe^{3+}/\sum Fe$. However, oxidation state of iron may be playing the larger role in determining mineral–melt equilibrium iron isotope fractionation. While oxidation state is often accompanied by a change in coordination number, in the case of mineral–melt equilibration, there is likely a coordination change for both Fe^{3+} and Fe^{2+}, implying it is the valence that controls the differences in bond strength.
5. The ionic model may be used to make predictions as to expectations for the sign and general magnitude of Fe isotope fractionation between minerals at equilibrium, but experiments must be done in order to confirm or refute the results of all existing models of temperature dependence of Fe equilibrium fractionation in mantle minerals.

ACKNOWLEDGEMENTS

APPENDIX A. SUPPLEMENTARY DATA

Supplementary data associated with this article can be found, in the online version, at http://dx.doi.org/10.1016/j.gca.2015.01.024.

REFERENCES

Ballhaus C., Berry R. F. and Green D. H. (1991) High pressure experimental calibration of the olivine–orthopyroxene–spinel oxygen geobarometer: implications for the oxidation state of the upper mantle. *Contrib. Miner. Petrol.* **107**(1), 27–40.

Beard B. L. and Johnson C. M. (2004) Inter-mineral Fe isotope variations in mantle-derived rocks and implications for the Fe geochemical cycle. *Geochim. Cosmochim. Acta* **68**, 4727–4743.

Bernatowicz T. J. (1981) Noble gases in ultramafic xenoliths from San Carlos, Arizona. *Contrib. Miner. Petrol.* **76**, 84–91.

Bigeleisen J. and Mayer M. G. (1947) Calculation of equilibrium constants for isotopic exchange reactions. *J. Chem. Phys.* **15**, 261–267.

Blanchard M., Poitrasson F., Meheut M., Lazzeri M., Mauri F. and Balan E. (2009) Iron isotope fractionation between pyrite (FeS_2), hematite ($Fe_2 O_3$) and siderite ($FeCO_3$): a first-principles density functional theory study. *Geochim. Cosmochim. Acta* **73**, 6565–6578.

Born M. and Mayer J. E. (1932) Zur Gittertheorie der Ionenkristalle. *Z. Phys. A Hadrons Nucl.* **75**, 1–18.

Canil D., O'Neill H., St C., Pearson D. G., Rudnick R. L., McDonough W. F. and Carswell D. A. (1994) Ferric iron in peridotites and mantle oxidation states. *Earth Planet. Sci. Lett.* **123**, 205–220.

Dauphas N., Craddock P. R., Asimow P. D., Bennett V. C., Nutman A. P. and Ohnenstetter D. (2009) Iron isotopes may reveal the redox conditions of mantle melting from Archean to Present. *Earth Planet. Sci. Lett.* **288**, 255–267.

Deer W. A., Howie R. A. and Zussman J. (1992) *An introduction to the rock-forming minerals* (vol. 2) Hong Kong: Longman Scientific & Technical.

Feng C., Qin T., Huang S., Wu Z. and Huang F. (2014) First-principles investigations of equilibrium calcium isotope fractionation between clinopyroxene and Ca-doped orthopyroxene. *Geochim. Cosmochim. Acta* **143**, 132–142.

Frey F. A. and Green D. H. (1974) The mineralogy, geochemistry and origin of lherzolite inclusions in Victorian basanites. *Geochim. Cosmochim. Acta* **38**(7), 1023–1059.

Frey F. A. and Prinz M. (1978) Ultramafic inclusions from San Carlos, Arizona: petrologic and geochemical data bearing on their petrogenesis. *Earth Planet. Sci. Lett.* **38**, 129–176.

Galer S. J. G. and O'Nions R. K. (1989) Chemical and isotopic studies of ultramafic inclusions from the San Carlos Volcanic Field, Arizona: a bearing on their petrogenesis. *J. Petrol.* **30**, 1033–1064.

Ghiorso M. S., Hirschmann M. M., Reiners P. W. and Kress, III, V. C. (2002) The pMELTS: a revision of MELTS for improved

calculation of phase relations and major element partitioning related to partial melting of the mantle to 3 GPa. *Geochem. Geophys. Geosyst.* **3**, 1–35.

Gregory and Criss (1986) Isotopic exchange in open and closed systems. *Rev. Mineral. Geochem.* **16**, 91–128.

Gudfinnsson G. H. and Presnall D. C. (2000) Melting behavior of model lherzolite in the system CaO–MgO–Al₂O₃–SiO₂–FeO at 0.7–2.8 GPa. *J. Petrol.* **41**, 1241–1269.

Holloway J. R. and Cross C. (1978) The San Carlos alkaline rock association. Geological Society of America Cordilleran Section Special Paper 2, pp. 171–173.

Huang S., Farkaš J. and Jacobsen S. B. (2010) Calcium isotopic fractionation between clinopyroxene and orthopyroxene from mantle peridotites. *Earth Planet. Sci. Lett.* **292**, 337–344.

Huang F., Zhang Z., Lundstrom C. C. and Zhi X. (2011) Iron and magnesium isotopic compositions of peridotite xenoliths from Eastern China. *Geochim. Cosmochim. Acta* **75**, 3318–3334.

Jackson W. E., Farges F., Yeager M., Mabrouk P. A., Rossano S., Waychunas G. A. and Brown G. E. (2005) Multi-spectroscopic study of Fe (II) in silicate glasses: Implications for the coordination environment of Fe (II) in silicate melts. *Geochim. Cosmochim. Acta* **69**(17), 4315–4332.

Jaques A. L. and Green D. H. (1980) Anhydrous melting of peridotite at 0–15 kb pressure and the genesis of tholeiitic basalts. *Contrib. Miner. Petrol.* **73**, 287–310.

Jeffcoate A. B., Elliott T., Kasemann S. A., Ionov D., Cooper K. and Brooker R. (2007) Li isotope fractionation in peridotites and mafic melts. *Geochim. Cosmochim. Acta* **71**, 202–218.

Kelemen P. B., Shlmlzu N. and Saltersi V. J. (1995) Extraction of mid-ocean-ridge basalt from the upwelling mantle by focused flow of. *Nature* **375**, 29.

Kinzler R. J. (1997) Melting of mantle peridotite at pressures approaching the spinel to garnet transition: application to mid-ocean ridge basalt petrogenesis. *J. Geophys. Res.* **102**, 853–874.

Klein C., Hurlbut C. S. and Dana J. D. (1993). .

Kyser T. K. (1990) Stable isotopes in the continental lithospheric mantle. *Cont. Mantle* **2**(3C), 127.

Macris C. A. and Manning C. E. (2006) The solubility of diopside in H₂O–NaCl fluids at 800 °C and 10 kbar. In *AGU Fall Meeting Abstracts* (vol. 1, p. 1091).

Mattey D., Lowry D. and Macpherson C. (1994) Oxygen isotope composition of mantle peridotite. *Earth Planet. Sci. Lett.* **128**(3), 231–241.

Menzies M. (2003) Mantle ultramafic xenoliths in alkaline magmas: evidence for mantle heterogeneity modified by magmatic activity. In *Continental Basalts and Mantle Xenoliths* (eds. C. J. Hawkesworth and M. J. Norry). Shiva, Cheshire, pp. 92–110.

Newton R. C. and Manning C. E. (2006) Solubilities of corundum, wollastonite and quartz in H₂O–NaCl solutions at 800 ° C and 10 kbar: interaction of simple minerals with brines at high pressure and temperature. *Geochim. Cosmochim. Acta* **70**, 5571–5582.

Pauling L. (1929) The principles determining the structure of complex ionic crystals. *J. Am. Chem. Soc.* **51**, 1010–1026.

Perkins G. B., Sharp Z. D. and Selverstone J. (2006) Oxygen isotope evidence for subduction and rift-related mantle metasomatism beneath the Colorado Plateau-Rio Grande rift transition. *Contrib. Miner. Petrol.* **151**(6), 633–650.

Poitrasson F., Halliday A. N., Lee D. C., Levasseur S. and Teutsch N. (2004) Significance of iron isotope mineral fractionation in pallasites and iron meteorites for the core–mantle differentiation of terrestrial planets. *Earth Planet. Sci. Lett.* **223**, 253–266.

Poitrasson F., Delpech G. and Gregoire M. (2013) On the iron isotope heterogeneity of lithospheric mantle xenoliths: implica-

tions for mantle metasomatism, the origin of basalts and the iron isotope composition of the Earth. *Contrib. Miner. Petrol.* **165**, 1243–1258.

Polyakov V. B. (1997) Equilibrium fractionation of the iron isotopes: estimation from Mossbauer spectroscopy data. *Geochim. Cosmochim. Acta* **61**, 4213–4217.

Polyakov V. B. and Mineev S. D. (2000) The use of Mössbauer spectroscopy in stable isotope geochemistry. *Geochim. Cosmochim. Acta* **64**, 849–865.

Polyakov V. B., Clayton R. N., Horita J. and Mineev S. D. (2007) Equilibrium iron isotope fractionation factors of minerals: reevaluation from the data of nuclear inelastic resonant X-ray scattering and Mössbauer spectroscopy. *Geochim. Cosmochim. Acta* **71**, 3833–3846.

Rustad J. R. and Dixon D. A. (2009) Prediction of iron-isotope fractionation between hematite (α-Fe₂O₃) and ferric and ferrous iron in aqueous solution from density functional theory. *J. Phys. Chem. A* **113**(44), 12249–12255.

Sachtleben T. and Seck H. A. (1981) Chemical control of Al-solubility in orthopyroxene and its implications on pyroxene geothermometry. *Contrib. Mineral. Petrol.* **78**(2), 157–165.

Schauble E. A. (2004) Applying stable isotope fractionation theory to new systems. *Rev. Mineral. Geochem.* **55**, 65–111.

Schauble E. A. (2011) First-principles estimates of equilibrium magnesium isotope fractionation in silicate, oxide, carbonate and hexaaquamagnesium(2+) crystals. *Geochim. Cosmochim. Acta* **75**, 844–869.

Schoenberg R. and von Blanckenburg F. (2006) Modes of planetary-scale Fe isotope fractionation. *Earth Planet. Sci. Lett.* **252**, 342–359.

Schuessler J. A., Schoenberg R., Behrens H. and von Blanckenburg F. (2007) The experimental calibration of the iron isotope fractionation factor between pyrrhotite and peralkaline rhyolitic melt. *Geochim. Cosmochim. Acta* **71**(2), 417–433.

Shannon R. T. (1976) Revised effective ionic radii and systematic studies of interatomic distances in halides and chalcogenides. *Acta Crystallogr., Sect. A* **32**(5), 751–767.

Takahashi E. and Kushiro I. (1983) Melting of a dry peridotite at high pressures and basalt magma genesis. *Am. Mineral.* **68**, 859–879.

Urey H. C. (1947) The thermodynamic properties of isotopic substances. *J. Chem. Soc.*, 562–581.

Wan Z., Coogan L. A. and Canil D. (2008) Experimental calibration of aluminum partitioning between olivine and spinel as a geothermometer. *Am. Mineral.* **93**(7), 1142–1147.

Walter M. J. and Presnall D. C. (1994) Melting behavior of simplified lherzolite in the system CaO–MgO–Al₂O₃–SiO₂–Na₂O from 7 to 35 kbar. *J. Petrol.* **35**, 329–359.

Weyer S. and Ionov D. A. (2007) Partial melting and melt percolation in the mantle: the message from Fe isotopes. *Earth Planet. Sci. Lett.* **259**, 119–133.

Weyer S. and Schwieters J. B. (2003) High precision Fe isotope measurements with high mass resolution MC-ICPMS. *Int. J. Mass Spectrom.* **226**, 355–368.

Weyer S., Anbar A. D., Brey G. P., Munker C., Mezger K. and Woodland A. B. (2005) Iron isotopic fractionation during planetary differentiation. *Earth Planet. Sci. Lett.* **240**, 251–264.

Wilke M., Partzsch G. M., Bernhardt R. and Lattard D. (2005) Determination of the iron oxidation state in basaltic glasses using XANES at the K-edge. *Chem. Geol.* **220**(1), 143–161.

Williams H. M. and Bizimis M. (2014) Iron isotope tracing of mantle heterogeneity within the source regions of oceanic basalts. *Earth Planet. Sci. Lett.* **404**, 396–407.

Williams H. M., McCammon C. A., Peslier A. H., Halliday A. N., Teutsch N., Levasseur S. and Burg J.-P. (2004) Iron isotope

fractionation and the oxygen fugacity of the mantle. *Science* **304**, 1656–1659.

Williams H. M., Pelsier A. H., McCammon C., Halliday A. N., Levasseur S., Teutsch N. and Burg J.-P. (2005) Systematic iron isotope variations in mantle rocks and minerals: the effects of partial melting and oxygen fugacity. *Earth Planet. Sci. Lett.* **235**, 435–452.

Williams H. M., Nielsen S. G., Renac C., Griffin W. L., O'Reilly S. Y., McCammon C. A., Pearson N., Viljoen F., Alt J. C. and Halliday A. N. (2009) Fractionation of oxygen and iron isotopes by partial melting processes: implications for the interpretation of stable isotope signatures in mafic rocks. *Earth Planet. Sci. Lett.* **283**, 155–166.

Woodland A. B., Kornprobst J. and Tabit A. (2006) Ferric iron in orogenic lherzolite massifs and controls of oxygen fugacity in the upper mantle. *Lithos* **89**, 222–241.

Wykes J. L., Newton R. C. and Manning C. E. (2011) Forsterite solubility in NaCl–H_2O fluids at upper mantle PT conditions. In *AGU Fall Meeting Abstracts* (vol. 1, p. 0059).

Young E. D., Galy A. and Nagahara H. (2002) Kinetic and equilibrium mass-dependent isotope fractionation laws in nature and their geochemical and cosmochemical significance. *Geochim. Cosmochim. Acta* **66**, 1095–1104.

Young E. D., Tonui E., Manning C. E., Schauble E. and Macris C. A. (2009) Spinel–olivine magnesium isotope thermometry in the mantle and implications for the Mg isotopic composition of Earth. *Earth Planet. Sci. Lett.* **288**, 524–533.

Zhao X., Zhang H., Zhu X., Tang S. and Tang Y. (2010) Iron isotope variations in spinel peridotite xenoliths from North China Craton: implications for mantle metasomatism. *Contrib. Miner. Petrol.* **160**, 1–14.

Zhao X., Zhang H., Zhu X., Tang S. and Yan B. (2012) Iron isotope evidence for multistage melt-peridotite interactions in the lithospheric mantle of eastern China. *Chem. Geol.* **292–293**, 127–139.

Zhu X. K., Guo Y., Williams R. J. P., O'Nions R. K., Matthews A., Belshaw N. S., Canters G. W., de Waal E. C., Weser U., Burgess B. K. and Salvato B. (2002) Mass fractionation processes of transition metal isotopics. *Earth Planet. Sci. Lett.* **200**, 47–62.

Associate editor: Shichun Huang